Article

Immunity

Structural Activation of Pro-inflammatory Human Cytokine IL-23 by Cognate IL-23 Receptor Enables Recruitment of the Shared Receptor IL-12Rβ1

Graphical Abstract

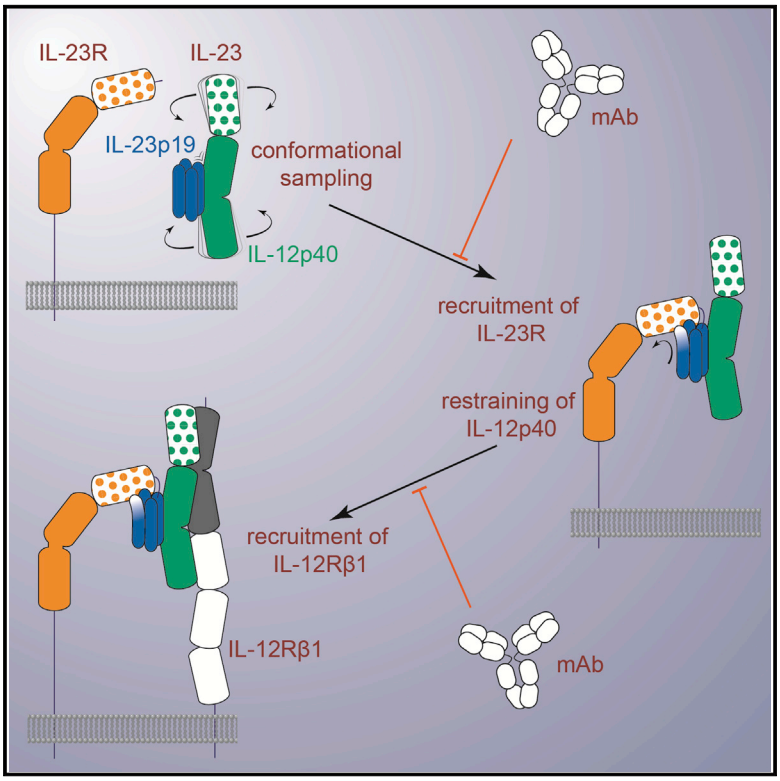

Highlights

- Determined crystal structure of human IL-23 in complex with cognate IL-23R
- IL-23 is restrained upon IL-23R binding to enable recruitment of IL-12Rβ1
- A single residue in IL-23 is crucial for its pro-inflammatory activity
- Receptor binding sites on IL-23 segregate to the p19 and p40 subunits

Authors

Yehudi Bloch, Laura Bouchareychas, Romain Merceron, ..., Melissa Dullaers, Iannis E. Adamopoulos, Savvas N. Savvides

Correspondence

savvas.savvides@ugent.be

In Brief

IL-23, a human cytokine under intense clinical targeting, is pivotal to cellular responses underlying widespread inflammatory and autoimmune diseases, such as psoriasis and rheumatoid arthritis. Bloch et al. determine the structure of IL-23 bound by one of its receptors, IL-23R, and reveal how IL-23R activates IL-23 for recruiting IL-12Rβ1 to the signaling assembly. Together with identifying an interaction hotspot, such findings may contribute to additional approaches for the mechanistic and therapeutic interrogation of receptor complexes mediated by IL-12 family members.

Bloch et al., 2018, Immunity *48*, 45–58
January 16, 2018
https://doi.org/10.1016/j.immuni.2017.12.008

CellPress

Immunity
Article

Structural Activation of Pro-inflammatory Human Cytokine IL-23 by Cognate IL-23 Receptor Enables Recruitment of the Shared Receptor IL-12Rβ1

Yehudi Bloch,[1,2] Laura Bouchareychas,[3,4,9] Romain Merceron,[1,2] Katarzyna Składanowska,[1,2] Lien Van den Bossche,[5,6] Sammy Detry,[1,2] Srinath Govindarajan,[2,7] Dirk Elewaut,[2,7] Filomeen Haerynck,[5,6,8] Melissa Dullaers,[5,6,7] Iannis E. Adamopoulos,[3,4] and Savvas N. Savvides[1,2,10,*]

[1]Laboratory for Protein Biochemistry and Biomolecular Engineering, Department of Biochemistry and Microbiology, Ghent University, 9052 Ghent, Belgium
[2]VIB-UGent Center for Inflammation Research, 9052 Ghent, Belgium
[3]Department of Internal Medicine, Division of Rheumatology, Allergy and Clinical Immunology, University of California at Davis, Davis, CA 95616, USA
[4]Institute for Pediatric Regenerative Medicine, Shriners Hospitals for Children Northern California, Sacramento, CA 95817, USA
[5]Clinical Immunology Research Lab, Department of Pulmonary Medicine, Ghent University Hospital, 9000 Ghent, Belgium
[6]Center for Primary Immunodeficiency, Jeffrey Modell Diagnosis and Research Centre, Ghent University Hospital, 9000 Ghent, Belgium
[7]Laboratory for Molecular Immunology and Inflammation, Department of Rheumatology, Ghent University Hospital, 9000 Ghent, Belgium
[8]Department of Pediatrics, Division of Pediatric Immunology and Pulmonology, Ghent University Hospital, 9000 Ghent, Belgium
[9]Present address: Division of Vascular and Endovascular Surgery, Department of Surgery, University of California San Francisco and Veterans Affairs Medical Center, San Francisco, CA 94143, USA
[10]Lead Contact
*Correspondence: savvas.savvides@ugent.be
https://doi.org/10.1016/j.immuni.2017.12.008

SUMMARY

Interleukin-23 (IL-23), an IL-12 family cytokine, plays pivotal roles in pro-inflammatory T helper 17 cell responses linked to autoimmune and inflammatory diseases. Despite intense therapeutic targeting, structural and mechanistic insights into receptor complexes mediated by IL-23, and by IL-12 family members in general, have remained elusive. We determined a crystal structure of human IL-23 in complex with its cognate receptor, IL-23R, and revealed that IL-23R bound to IL-23 exclusively via its N-terminal immunoglobulin domain. The structural and functional hotspot of this interaction partially restructured the helical IL-23p19 subunit of IL-23 and restrained its IL-12p40 subunit to cooperatively bind the shared receptor IL-12Rβ1 with high affinity. Together with structural insights from the interaction of IL-23 with the inhibitory antibody briakinumab and by leveraging additional IL-23:antibody complexes, we propose a mechanistic paradigm for IL-23 and IL-12 whereby cognate receptor binding to the helical cytokine subunits primes recruitment of the shared receptors via the IL-12p40 subunit.

INTRODUCTION

IL-12 family cytokines (IL-12, IL-23, IL-27, IL-35) are predominantly produced by activated antigen-presenting cells, such as dendritic cells and activated macrophages, and act as key immunological playmakers to coordinate innate and adaptive immune responses mainly via regulation of T cell populations (Eberl, 2016; Hasegawa et al., 2016). Hallmarked by their heterodimeric nature and intriguing cross-utilization of cytokine subunits and sharing of signaling receptors, IL-12 family cytokines operate on opposing sides of the immunological balance. For instance, the archetypal IL-12 (Gubler et al., 1991; Wolf et al., 1991) and IL-23 (Oppmann et al., 2000) are charted as pro-inflammatory cytokines contrasting the rather protective roles of IL-27 and IL-35 (Vignali and Kuchroo, 2012).

IL-23 is an extensively studied member of the IL-12 family of cytokines. Heterodimeric IL-23 comprises a p19 helical-bundle subunit (IL-23p19), which is disulphide linked to a p40 subunit (IL-12p40) (Oppmann et al., 2000). The latter is shared with IL-12, thereby defining a key structural and functional divergence within the IL-12 family. For instance, IL-23 signals via its specific receptor interleukin-23 receptor (IL-23R) and interleukin-12 receptor subunit β1 (IL-12Rβ1), which is also utilized by IL-12 (Parham et al., 2002). Yet functionally, the two cytokines trigger diametrically opposite immunological pathways. IL-12 drives differentiation of naive T cells into interferon-γ (IFN-γ)-producing T helper 1 (Th1) cells in type 1 immunity, whereas IL-23 is synonymous with type 3 immune responses pivotal to the survival and expansion of $CD4^+$ T helper 17 (Th17) cells (reviewed by Eberl, 2016).

It is precisely the potency by which IL-23 can drive production of interleukin-17 (IL-17) by Th17 cells and IL-17-producing γδ T (γδT17) cells that has propelled IL-23 to a major therapeutic target (Gaffen et al., 2014). Indeed, IL-23R is required *in vivo* for effector Th17 cell responses (McGeachy et al., 2009), which are now closely associated with many autoimmune and chronic inflammatory disorders, including psoriasis, psoriatic arthritis, Crohn's disease, rheumatoid arthritis, multiple sclerosis,

inflammatory bowel disease, and uveitis (Duerr et al., 2006; Korn et al., 2009; Lowes et al., 2014; Lubberts, 2015; Murphy et al., 2003). Nevertheless, the IL-23-IL-17 axis appears to entail differential roles for the two cytokines in intestinal immunoregulation, as their inhibition in Crohn's disease yields opposing effects, with IL-23 emerging as the therapeutically relevant target (Lee et al., 2015; Maxwell et al., 2015). Furthermore, elevated expression of IL-23 and IL-23R (and IL-17A) has been observed in several cancers, such as those of the skin, lung, breast, and colon (Grivennikov et al., 2012; Langowski et al., 2006; Zhang et al., 2014). The therapeutic context of IL-23 targeting continues to grow as recently evidenced by strategies to treat and manage pustular psoriasis (Arakawa et al., 2016), pityriasis rubra pilaris (Feldmeyer et al., 2017), and inflamed lesions in patients with leukocyte adhesion deficiency type 1 (Moutsopoulos et al., 2017).

Despite the wealth of information on the immunoregulatory functions and disease-related context of IL-23 and IL-12 family cytokines, the field is characterized by a paucity of structural information. For instance, structural information of complexes of IL-12 family cytokines with cognate receptors is currently lacking. By elucidating the crystal structure of the IL-23:IL-23R complex and based on biochemical and biophysical undertakings, we here provided insights into how IL-23 becomes structurally primed by IL-23R to mediate a tripartite complex with IL-12Rβ1. Supported by functional interrogation of key interactions in a mouse model of skin inflammation and by consolidating emerging structure-function considerations, we propose a mechanism for the pro-inflammatory signaling complex mediated by IL-23. Restructuring of the helical IL-23p19 subunit of IL-23 as a result of its interaction with the N-terminal immunoglobulin (Ig) domain of IL-23R constitutes a mechanistic prerequisite, which leads to receptor-mediated restraining of the p40 subunit of IL-23 to enable a high-affinity interaction with the shared receptor IL-12Rβ1 in cooperative fashion. Thus, our mechanistic proposal segregates cognate and shared receptor binding to the helical (α) and non-helical (β) subunits of the heterodimeric cytokines in the IL-12 family, respectively.

RESULTS

Crystal Structure of the Human IL-23:IL-23R Complex

IL-23 signals via its cognate receptor IL-23R and the shared receptor IL-12Rβ1 and is thought to mediate a stoichiometric ternary complex with the ectodomains of the two receptors (Figure 1A). While IL-12Rβ1 orthologs consistently display five extracellular domains (Figure S1A), mammalian IL-23R consist of just three extracellular domains compared to evolutionarily more distant verterbrates, which have two to three additional membrane-proximal fibronectin type III (FnIII) domains (Figures S1B and S1C). Current models for the assembly of cell-surface complexes mediated by IL-12 family cytokines have been largely based on the structural principles derived from the interleukin-6 (IL-6) complex with interleukin-6 receptor subunit alpha (IL-6Rα) and glycoprotein 130 (gp130) and other gp130 complexes (Boulanger et al., 2003; Skiniotis et al., 2005).

Given the paucity of structural information for any IL-12 family complex and the growing importance of specific therapeutic targeting of human IL-23 (Teng et al., 2015), we pursued structural studies of human IL-23 and its complexes with the ectodomains of its specific receptor IL-23R and the shared receptor IL-12Rβ1 (Figure 1A). We produced recombinant human IL-23 and the ectodomains of IL-23R (residues 1–317) and IL-12Rβ1 (residues 1–540) (Figure 1A) via inducible stable expression and secretion in HEK293S *MGAT1*$^{-/-}$ cells, which limit N-linked glycosylation of proteins to $Man_5GlcNAc_2$ glycan trees (Reeves et al., 2002; Verstraete et al., 2011). We biochemically reconstituted and purified stoichiometric IL-23:IL-23R binary and IL-23:IL-23R:IL-12Rβ1 ternary complexes to enable structural studies (Figures S2A–S2C). However, the IL-23:IL-23R:IL-12Rβ1 ternary complex displayed low stability and solubility. On the other hand, the IL-23:IL-23R binary complex proved much more amenable to structural studies and initially led to poorly diffracting crystals (~20 Å resolution). To improve crystal quality, we leveraged a collection of single-domain VHH camelid antibodies targeting human IL-23 (Saunders et al., 2009) (PDB: 3qwr). Introduction of Nb22E11 to the IL-23:IL-23R complex yielded much improved crystals, which could be further optimized via shaving of N-linked glycans in purified IL-23:IL-23R:Nb22E11 complex by Jackbean α-mannosidase (Figures S2D and S2E). X-ray diffraction data from such crystals enabled structure determination of the complex to 2.8 Å resolution (Figures 1B–1F and S2F–S2I; Table 1).

The crystal structure of the IL-23:IL-23R:Nb22E11 complex provided structural insights into the IL-12 family of cytokine-receptor complexes. IL-23 deploys only its IL-23p19 subunit to contact IL-23R at its N-terminal Ig-like domain (D1), establishing a mixed interaction interface of ~900 Å^2 mediated by a total of 51 residues (Figures 1B–1F and S2I; Table S1). The two domains forming the cytokine-binding homology region (CHR) of IL-23R (D2 and D3) stayed clear of IL-23 and extended away from the cytokine-receptor interaction site via a nearly linear arrangement of D1 and D2, followed by a sharp bend at the D2-D3 linker to orient D3 at right angles to the plane formed by D1, D2, and IL-23p19 (Figures 1B and 1F). The CHR domains included the WSXWS motif in D3 (W304 Q305 P306 W307 S308) and adopted an inter-domain orientation reminiscent of CHR domains in the common gamma (γc) family of receptors (Verstraete et al., 2014; Wang et al., 2009). This motif formed a zipper-like arrangement of stacking interactions alternating between side chains in the motif and side chains on neighboring β strands along D3 (Figure S3A). W304 is also a putative C-mannosylation site, but no electron density was observed to support such post-translational modification. On the other hand, we observed clear electron density for six N-linked glycosylation sites in the ectodomain of human IL-23R at N47 and N81 in D1, two stacked glycans at N141 and N180 in D2, and at N262 and N273 in D3 (Figure 1B). Finally, previously reported glycosylation of N29 near the N terminus N29 (Zhao et al., 2010) was not supported by our experimental electron density and might be incompatible with the observed binding interface. Nanobody Nb22E11 binds at the junction of the two N-terminal domains of IL-12p40 (PDB: 3qwr), far away from the IL-23:IL-23R interaction site.

A limited interface (~290 Å^2) between D1 and D2 of IL-23R and an interface covering 480 Å^2 between D2 and D3 are in line with previously determined structures of type I cytokine receptors featuring an Ig-like domain linked to CHR domains, such as IL-12p40, gp130, and IL-6Rα. In IL-23R, D1 links to D2 by a nearly linear prolongation of the D1 G β strand leading into the

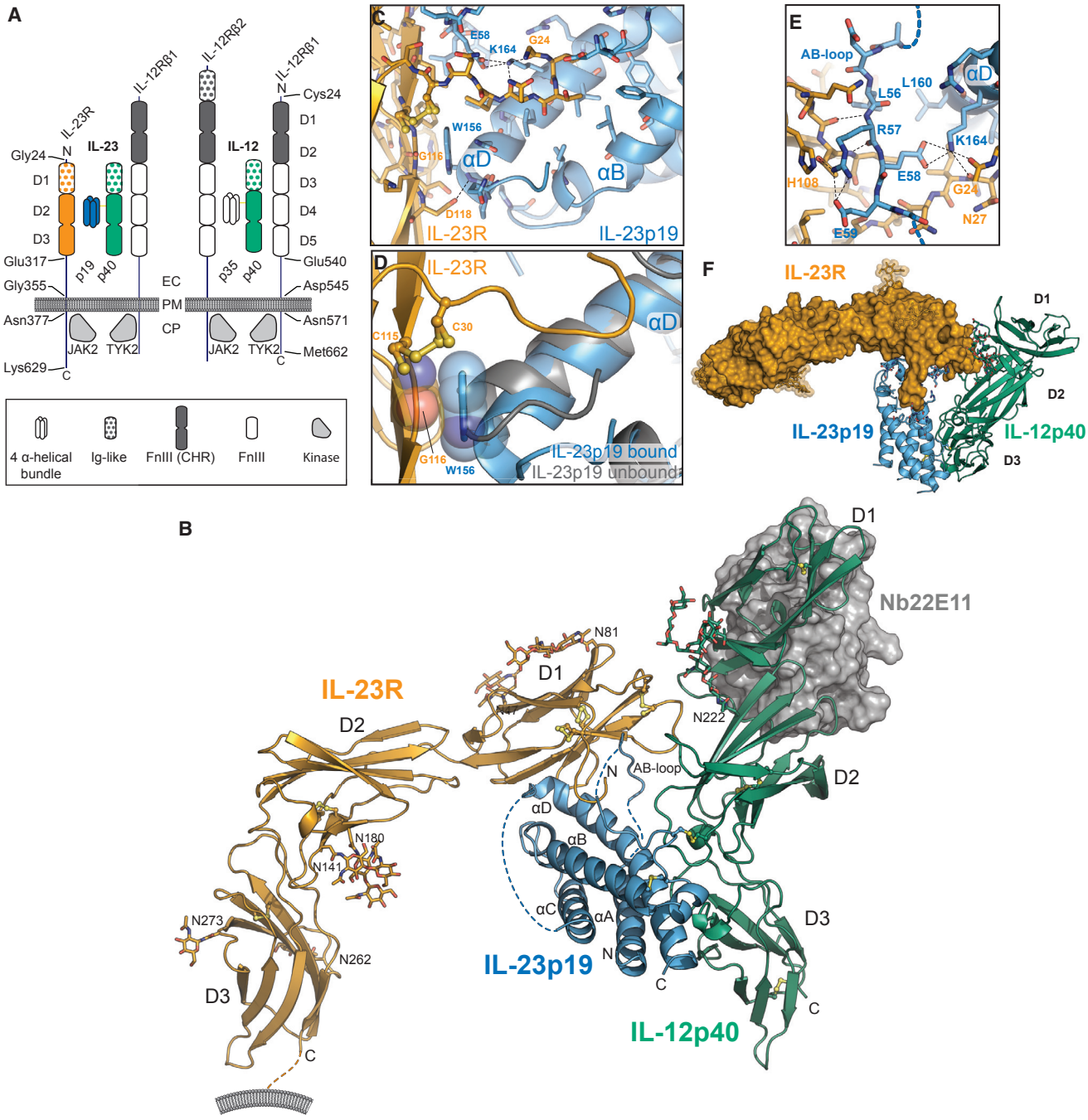

Figure 1. Structure of the IL-23:IL-23R Complex

(A) Schematic representation of protein components participating in IL-23 and IL-12 signaling complexes. Abbreviations are as follows: EC, extracellular; PM, plasma membrane; CP, cytoplasm; p19, IL-23p19; p40, IL-12p40.

(B) Cartoon representation of the IL-23:IL-23R crystal structure. Nanobody 22E11 used as a crystallization adjuvant is shown in gray surface representation.

(C) Close-up view of the IL-23R:IL-23p19 interface in the vicinity of W156 in IL-23p19.

(D) Restructuring of IL-23 upon binding to IL-23R.

(E) Close-up view of the interactions around the AB-loop of IL-23p19.

(F) Top-down view of the IL-23:IL-23R complex with IL-23R (surface).

See also Figures S1–S3 and Tables S1 and S2.

Table 1. Crystallographic Data and Refinement Statistics

Protein	IL-23:IL-23R:Nb22E11	IL-23	IL-23:Briakinumab^{Fab}	Briakinumab^{Fab}
PDB code	5mzv	5mxa	5njd	5n2k
Crystallization condition	0.2 M $MgCl_2$ 0.1 M Tris (pH 6.6) 11% (w/v) PEG8000	19.5% (w/v) PEG1000, 100 mM Citrate Phosphate (pH 4.4), 200 mM Li2SO4	2 M $(NH_4)_2SO_4$, 100 mM BisTris (pH 6)	200 mM NH_4I, 20% (w/v) PEG3350 (pH 6.2)
Cryo-protectant	20% ethylene glycol	5% PEG1000	saturated $(NH_4)_2SO_4$	20% ethylene glycol
Data Collection[a]				
Beamline	PetraIII-P14	PetraIII-P14	PetraIII-P14	PetraIII-P14
Wavelength	0.98 Å	0.98 Å	0.98 Å	0.98 Å
Space Group	P 2_1	P 6_1	P 4_12_12	P 2_1
a,b,c (Å)	67.22, 112.19, 109.87	109.80, 109.80, 87.69	191.61, 191.61, 519.11	85.25, 172.54, 138.16
α,β,γ (°)	90.0, 106.24, 90.0	90, 90, 120	90, 90, 90	90.0, 106.16, 90.0
Resolution (Å)	76.9–2.8 (2.9–2.8)	87.7–2.5 (2.65–2.50)	95.8–3.9 (4.14–3.90)	81.88–2.22 (2.34–2.22)
Total reflections	131,247 (13,351)	213,965 (33,428)	439,822 (66,604)	732,035 (110,384)
Unique reflections	38,061 (3,803)	20,825 (3,297)	86,556 (13,014)	178,979 (26,837)
Multiplicity	3.4 (3.5)	10.3 (10.1)	5.1 (5.1)	4.1 (4.1)
Completeness (%)	98.4 (99.2)	99.7 (98.2)	97.7 (92.5)	94.7 (96.5)
Mean I/σ(I)	12.4 (2.8)	24.6 (2.2)	4.2 (1.2)	8.9 (2.2)
Wilson B-factor (Å^2)	72.2	69.4	N/A	53.4
R-meas (%)	8.1 (52.8)	6.6 (103.1)	43.8 (137.8)	11.0 (91.7)
CC1/2 (%)	99.7 (63.4)	100 (73.1)	96.0 (43.0)	99.5 (68.6)
Refinement[b]				
Resolution range (Å)	76.9–2.8 (2.9–2.8)	64.5–2.5 (2.59–2.50)	95.8–3.9 (4.05–3.9)	81.9–2.22 (2.30–2.22)
Reflections in refinement	38,058 (3,805)	20,823 (2,020)	86,486 (7,722)	178,458 (17,823)
Reflections used for R-free	1,594 (156)	1,716 (165)	1,835 (165)	2,153 (215)
R-work	0.211 (0.319)	0.187 (0.290)	0.273 (0.358)	0.203 (0.281)
R-free	0.249 (0.321)	0.226 (0.347)	0.313 (0.354)	0.233 (0.323)
Non-hydrogen atoms	7,116	3,484	39,446	26,313
Macromolecular atoms	6,803	3,398	39,015	25,304
Ligands	238	50	431	4
Protein residues	856	441	5,146	3,382
RMS(bonds) (Å)	0.003	0.009	0.004	0.003
RMS(angles) (°)	0.65	0.91	0.57	0.61
Ramachandran favored (%)	94	97	94	97
Ramachandran allowed (%)	6.2	3.3	5.6	2.7
Ramachandran outliers (%)	0	0	0.4	0.09
Rotamer outliers (%)	0.5	1.1	0.3	0.5
Clashscore	1.1	1.2	1.2	1.1
Average B-factor (Å^2)	84.5	79.5	120.1	63.80
macromolecules	83.4	79.6	120.2	64.4
ligands	123.8	88.2	106.7	52.2
solvent	57.7	57.1	–	49.1
TLS groups	14	10	24	33

[a]Values reported by XDS.
[b]Values reported by Phenix.

A β strand in D2, consistent with proposals that such minimal interfaces between D1 and D2 may facilitate inter-domain plasticity (Skiniotis et al., 2005). The D2:D3 interface, however, is not only larger but also stabilized by several hydrogen bonds and salt bridges (Table S1). The relative orientation of D2 and D3 is rather well conserved among type I cytokine receptors, consistent with the cytokine binding function of the elbow region between D2 and D3 in other receptors. Thus, the binary complex of IL-23 with IL-23R provided insights into the possible structural plasticity and role of the three extracellular domains of IL-23R in binding the cytokine and the key conclusion that the N-terminal Ig domain of IL-23R serves as the sole cytokine-binding domain.

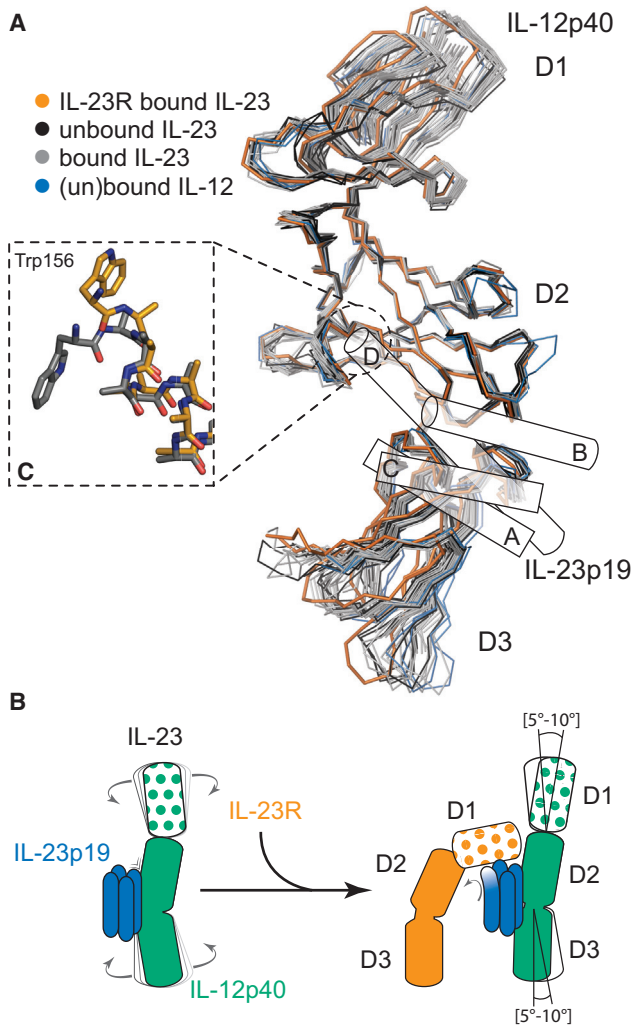

Figure 2. Conformational Selection in IL-23 upon IL-23R Binding

(A) Structural superposition of IL-12 p40 subunits as visualized in all available crystal structures (herein and PDB: 1f42, 1f45, 3d85, 3d87, 3duh, 3hmx, 3qwr, 4grw, 5mj3, and 5mj4) with respect to the D2 domain.

(B) Schematic recapitulation of the IL-23:IL-23R binding event.

(C) Structural transition of the N terminus of helix D in IL-23p19 from a canonical α-helix (gray, PDB: 5mj3) to a 3_{10} helix (orange) in the IL-23:IL-23R complex.

Recruitment of IL-23R Restructures IL-23

To address possible conformational changes in human IL-23 upon binding to IL-23R receptor and to enable appropriate structural comparisons, we acquired an additional snapshot of the structure of unbound IL-23 by crystallizing glycosylated human IL-23 produced in HEK293S *MGAT1*$^{-/-}$ cells (Table 1; Figure 1D; Shirouzono et al., 2012).

Arguably, the hallmarks of the IL-23:IL-23R interaction interface are threefold and feature conformational changes in both the cytokine and the receptor. First, IL-23 did not bind to the CHR domains of IL-23R, a mode of interaction commonly displayed by members of the cytokine superfamily activating type I cytokine receptors (Figure 1B). Second, the five N-terminal residues of D1 of IL-23R (G24–N29) that are not part of its canonical Ig fold adopted a hook-like structure tethered at the disulfide bridge defined by C30-C115 and reached out into the loops atop helices B and D of IL-23p19 (Figures 1C and 1F). This led to partial ordering of the loop linking helices A and B (AB loop) in IL-23p19 (residues 54–60) (Figure 1E). The indole ring of W156 at the N-terminal end of helix D in IL-23p19 stacked tightly against the peptide plane of G116 in the G β strand of IL-23R_{D1} (Figures 1D, S3B, and S3C). Interestingly, the IL-6:gp130 interface displays a very similar interaction based on conserved residues (Figure S1D; Boulanger et al., 2003). The interaction in the IL-23:IL-23R complex featured additional stabilizing interactions via hydrogen bonds between the main chain amide nitrogen of W156 in IL-23p19 and residue D118 in IL-23R. Third, W156 marked the end point of a restructuring of the N-terminal end of helix D in IL-23p19, which transitioned from a canonical α helix to a 3_{10}-helix (Figures 1D, 2C, S3B, and S3C) upon binding IL-23R. This 3_{10} helical conformation has also been observed in IL-23 in complex with a Fab fragment derived from the monoclonal antibody 7G10 targeting IL-23p19 (PDB: 3d85) (Beyer et al., 2008). In that case, W156 was located just at the edge of the Fab:IL-23 interaction epitope, highlighting the local conformational plasticity centered at W156 on helix D in IL-23p19.

Even though the epicenter of the IL-23:IL-23R interaction was the interface between IL-23R_{D1} and IL-23p19, IL-23R_{D1} also contacted IL-12p40 close to the D1 D2 interface, albeit to a very limited extent (260 Å^2). This interface was characterized by rather loose van der Waals contacts and only a single well-defined residue-residue interaction, namely, the bifurcated interaction of the guanidine group of R62 in IL-23R_{D1} with the side and main chain of D109 in IL-12p40 at the periphery of the interaction interface. A comprehensive listing of all the interactions observed at the IL-23:IL-23R interface can be found in Table S1.

Despite the limited footprint of IL-23R at the D1-D2 interface of IL-12p40, we wondered about the impact of IL-23R recruitment on the overall domain structure of IL-12p40. To this end we carried out structural superpositions with respect to D2 of all available structures of IL-12p40, including in the unbound form (PDB: 3d87 and 3duh). We found that IL-12p40 displayed extensive domain flexibility (Figure 2A) manifested by a hinge-like motion of D1 or D3 of 5°–10° with respect to D2. IL-12p40 in the context of its complex with IL-23R adopts the most extreme conformation, whereby D1 of IL-12p40 turns away from D2 and D3 swings toward IL-23p19 (Figure 2B). Together, the structural rearrangements at the IL-23:IL-23R interaction interface and the ensuing conformational restraining of the p40 subunit of IL-23 point to pronounced receptor-mediated restructuring events in IL-23 that may have mechanistic implications.

A Functional Hotspot in IL-23 Underlies High-Affinity Binding to IL-23R

We tapped into the structural insights from the IL-23:IL-23R complex to interrogate the possible functional relevance of interactions observed at the IL-23:IL-23R interface. In particular, we aimed to investigate whether mutagenesis of W156 in IL-23p19 at the heart of the interaction interface (Figures 1D and 2C) would manifest a strong phenotype in pro-inflammatory Th17-cell-relevant readouts *in vitro* and in skin inflammation *in vivo*. This is because the functional role of this particular position had been postulated based on structural considerations of the

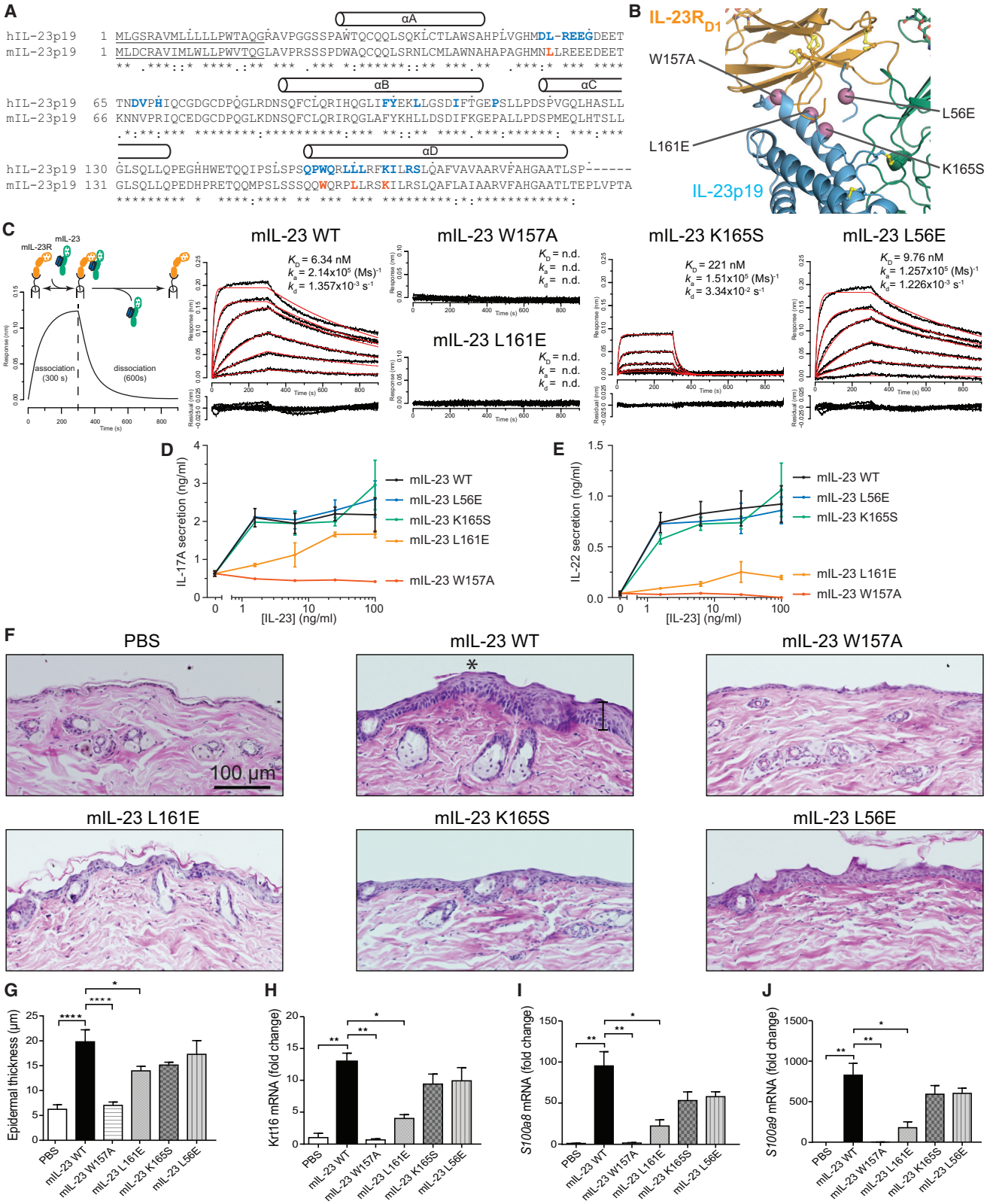

Figure 3. W157 in Mouse IL-23p19 Is a Functional Hotspot

(A) Sequence alignment of human and mouse IL-23p19. Residues at the human IL-23:IL-23R interface and positions chosen for mutagenesis in mouse IL-23 are shown in blue and red, respectively. Predicted secretion signal sequences are underlined.

(legend continued on next page)

receptor-free cytokine (Lupardus and Garcia, 2008) and has only recently been probed via reporter cellular assays *in vitro* (Schröder et al., 2015). Furthermore, W156 participated in interaction interfaces between IL-23 and therapeutic biologics and designed protein scaffolds (Figure 2A; Beyer et al., 2008; Desmet et al., 2014; Li et al., 2017). We further selected L56 and L160 in human IL-23p19, which become buried at the complex interface, as well as K164, which interacts with the main chain carbonyl oxygens of G24 and N27 of IL-23R and was further stabilized by E58 in IL-23p19 (Figures 1C and 1E).

Following structure-based sequence alignments to identify the equivalent amino acid positions in mouse IL-23 (Figures 3A and 3B), we produced and purified recombinant wild-type mouse IL-23 (mIL-23^{WT}) and mutant variants mIL-23p19^{W157A}, mIL-23p19^{L161E}, mIL-23p19^{K165S}, and mIL-23p19^{L56E}. The biochemical behavior and stability of all purified targeted mutant variants of mouse IL-23 were very similar to IL-23^{WT}. To assess the affinity of the mutant variants to mouse IL-23R (mIL-23R), we employed bio-layer interferometry (BLI) and found that mIL-23p19^{W157A} and mIL-23p19^{L161E} were unable to engage into a measurable interaction with mIL-23R compared to the high affinity displayed by mouse IL-23^{WT} (Figure 3C). The recombinant human IL-23 had similar binding affinity and kinetics to mIL-23R (Figure S5A). On the other hand, mIL-23p19^{K165S} showed moderately impaired affinity to the receptor, while binding of mIL-23p19^{L56E} was very comparable to mIL-23^{WT} (Figure 3C). We probed the cellular context of these findings by examining the secretion of IL-17A and interleukin-22 (IL-22), two key cytokines in skin inflammation, upon differentiation of conventional naive T cells into Th17 cells following stimulation by wild-type and mutant IL-23 variants. In each case, we found that mIL-23p19^{W157A} was unable to drive IL-17A and IL-22 secretion, with mIL-23p19^{L161E} also showing impaired activity (Figures 3D and 3E). The behavior of mIL-23p19^{L161E} in the cellular assays contrasts its apparent lack of binding to IL-23R in our BLI experiments. This suggests that the affinity of mIL-23p19^{L161E} for IL-23R is likely well into the micromolar range, which would be unmeasurable within the range of concentrations employed in our BLI experiments (2–500 nM). However, in a cellular context, where the dimensionality of the cell membrane and interactions with the shared receptor IL-12Rβ1 could serve as compensating parameters, mIL-23p19^{L161E} can exhibit measurable bioactivity. Thus, the lack of any measurable binding affinity and bioactivity for mIL-23p19^{W157A} *in vitro* mounts a strong case for the centrality of W157 on mIL-23 in the assembly of signaling complexes.

We sought to investigate the functional relevance of our structure-guided mutants of mIL-23 in a mouse model for skin inflammation in C57BL/6J mice. We established the working dose of mIL-23 via intradermal administration of mIL-23^{WT} at opposing sides of shaved dorsal skin for 4 consecutive days and by comparisons with topically applied imiquimod (IMQ), a known inducer of epidermal hyperplasia (Figures S4A–S4D). mIL-23 injections were sufficient to induce pathologic features, which included diffuse epidermal hyperplasia (acanthosis) with associated compact hyperkeratosis and parakeratosis of the stratum corneum and the formation of Munro's microabscesses (Figures S4B–S4D). These observations correlated with an upregulation of *Krt16* and *S100a8* mRNA expression levels on day 4 (Figures S4E and S4F).

Next, we investigated the capacity of the mIL-23 mutants to elicit such skin pathologies. Mice treated with mIL-23^{WT} showed a marked thickening of epidermis and leukocyte infiltration compared to mice injected with PBS (Figure 3C). In contrast to mIL-23p19^{WT}, which presented with a pronounced thickening of epidermis and leukocyte infiltration, mIL-23p19^{W157A} exhibited a complete lack of pathologies and was indistinguishable from the control phenotype (Figures 3F and 3G). mIL-23p19^{L161E} showed a statistically significant decrease ($p < 0.05$) of epidermal hyperplasia with associated compact hyperkeratosis and parakeratosis of the stratum corneum when compared to IL-23p19^{W157A} (Figures 3F and 3G). Mutants mIL-23p19^{K165S} and mIL-23p19^{L56E} caused only mild skin pathologies and epidermal thickness that was quantified as statistically insignificant ($p > 0.05$) compared to mIL-23^{WT} (Figures 3F and 3G). Quantification of epidermal thickness showed that these histological changes were not significantly different compared to mIL-23^{WT} ($p > 0.05$) (Figures 3F and 3G). Finally, we verified the histological differences observed between the different mutants using quantitative reverse-transcription PCR analysis of dorsal skin tissue to quantify the expression of hyperproliferation markers, such as keratin-16, S100-A8, and S100-A9. Consistent with histology, *Krt16*, *S100a8*, and *S100a9* transcriptional levels were significantly decreased in mIL-23p19^{W157A} ($p < 0.01$) and mIL-23p19^{L161E} ($p < 0.05$) compared to mIL-23^{WT} (Figures 3H–3J). A non-significant trend was observed with mIL-23p19^{K165S} and mIL-23p19^{L56E}.

Therefore, our findings identify position W157 in mouse IL-23, and by extrapolation W156 in human IL-23, as a *bona fide* functional and structural hotspot that underlies high-affinity binding to IL-23R to trigger restructuring of IL-23 for signaling purposes.

(B) Structural context of interrogated positions (violet) at the human IL-23:IL-23R interface. Residue numbers according to mouse sequence.
(C) Experimental BLI setup and representative response curves fitted with a 1:1 binding model (red) to quantify the kinetics (k_a, k_d) and binding affinity (K_D) of wild-type and mutant mIL-23 to mIL-23R.
(D and E) IL-17A and IL-22 secretion by Th17 cells upon differentiation from purified naive CD4$^+$ T cells by the addition of mouse IL-23. Error bars represent the standard deviation calculated from a technical replicate.
(F) Representative H&E staining of cutaneous biopsies obtained from C57BL/6J mice treated with PBS, IL-23, or IL-23 mutants. Diffuse epidermal hyperplasia (acanthosis) with associated compact hyperkeratotic and parakeratosis of the stratum corneum caused by wild-type IL-23 is indicated with an asterisk. The vertical black bar in the mIL-23^{WT} panel indicates epidermal thickness measurement.
(G) Quantification of epidermal thickness by microscopy.
(H–J) Expression of *Krt16*, *S100a8*, and *S100a9* in the dorsal skin of C57BL/6J mice injected with PBS, IL-23, or IL-23 mutants. p values were determined using one-way ANOVA followed by Holm-Sidak's multiple comparisons test (*$p < 0.05$; **$p < 0.01$; ***$p < 0.001$; ****$p < 0.0001$). Data are presented as ± SEM; n = [3–6]. See also Figures S4 and S5A.

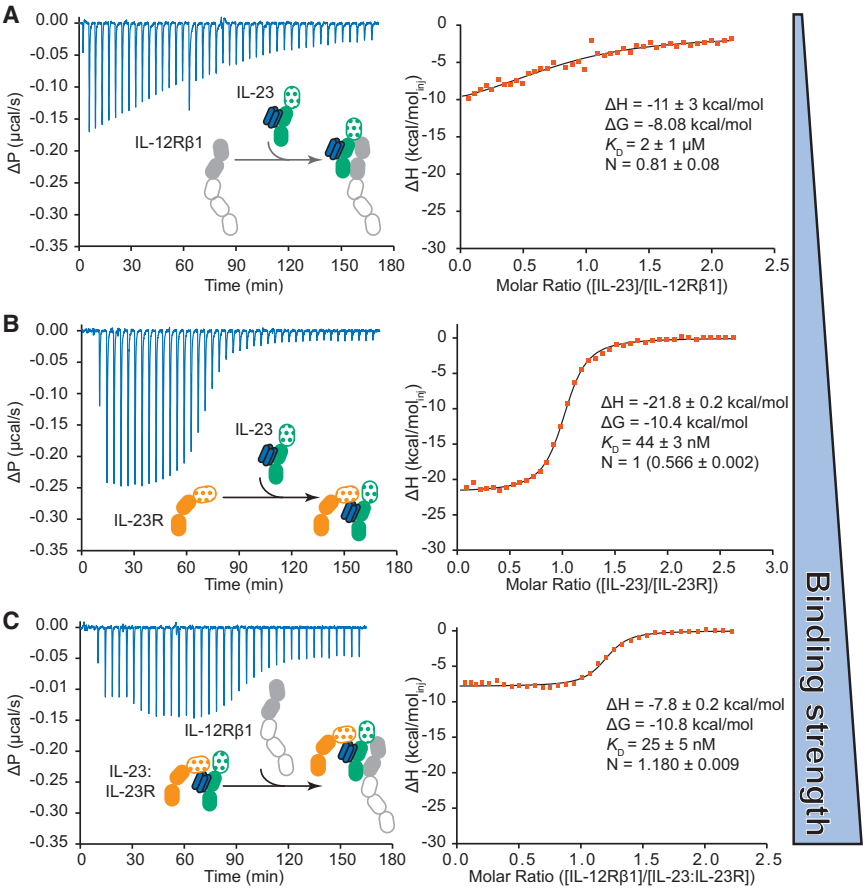

Figure 4. The IL-23:IL-23R Binary Complex Enables High-Affinity Binding of IL-12Rβ1

(A) Titration of IL-23 (72 μM) into IL-12Rβ1 (6.8 μM)

(B) Titration of IL-23 (55 μM) into IL-23R (6.5 μM). The stoichiometry of this experiment was set to 1 and the concentration in the cell was fitted to account for inactive IL-23R. The stoichiometry before correction is provided in parentheses.

(C) Titration of IL-12Rβ1 (38.8 μM) into preformed IL-23:IL-23R (3.6 μM). Fitted values are provided with their fitting errors.

See also Figure S5.

IL-23R Primes IL-23 for IL-12Rβ1 Recruitment

To draw the binding blueprint for the assembly of the human IL-23:IL-23R:IL-12Rβ1 complex, we employed purified recombinant human IL-23 and cognate receptor constructs in binding studies by microcalorimetry and characterized stoichiometric cytokine-receptor complexes by size exclusion chromatography coupled to inline multi-angle laser light scattering (SEC-MALLS). We first investigated the interaction capacity of the two receptors by titrating IL-23R into IL-12Rβ1 but were unable to measure any discernible binding (Figure S5B). We subsequently titrated IL-23 into either IL-12Rβ1 or IL-23R to establish the relative affinities of binary cytokine-receptor complexes. Whereas IL-23 binds to IL-12Rβ1 with an equilibrium dissociation constant (K_D) of 2 μM, its affinity for IL-23R is ~50-fold higher (K_D = 44 nM) (Figures 4A and 4B). The apparent binding in titrations with IL-23R does not obey a 1:1 stoichiometric ratio, suggesting that a fraction of recombinant IL-23R is inactive. This receptor fraction might be carrying an additional N-linked glycan at N29 (Zhao et al., 2010), which might prevent binding to IL-23p19 due to its proximity to the IL-23:IL-23R interaction site (Figures 1C and 1D).

We took advantage of our experimental setup to verify that the single domain VHH antibody we had used as a crystallization adjuvant does not affect the IL-23:IL-23R interaction. Indeed, titration of IL-23R into IL-23 and into a preformed complex of IL-23:Nb22E11 resulted in nearly identical binding profiles (Figures S5C and S5D). Furthermore, we sought to provide orthogonal evidence for the unexpected observation that the IL-23:IL-23R epitope involves only the Ig domain of IL-23R, in contrast to the employment of the CHR region in all other type I cytokine receptors characterized to date. Upon titrating IL-23R$_{D2D3}$ (residues G122-E317) into IL-23, we did not observe a binding event (Figure S5D), essentially confirming the delineation of the IL-23 binding epitope to the N-terminal Ig-domain of IL-23R. Despite multiple attempts we were unable to express a stand-alone IL-23R$_{D1}$ for binding studies.

Having concluded that our structural view of the IL-23:IL-23R complex is the high-affinity binary receptor complex of IL-23, we proceeded to titrate IL-12Rβ1 into preformed IL-23:IL-23R complex. IL-12Rβ1 could be recruited to this complex to form the ternary assembly with a K_D = 25 nM, i.e., a ~100-fold higher affinity compared to its binary interaction with IL-23 (Figure 4C). We corroborated this sequential assembly of a ternary complex by SEC-MALLS by supplementing purified IL-23:IL-23R binary complex with 1:1 stoichiometry with IL-12Rβ1, to show that IL-12Rβ1 can be recruited to a chromatographically distinct species bearing a molecular mass consistent with 1:1:1 stoichiometry (Figure S2B).

Together, our orthogonal experimental evidence for the assembly mechanism of the receptor complex mediated by IL-23 supports a sequential and cooperative process, whereby a stable binary IL-23:IL-23R complex is the mechanistic prerequisite for the recruitment of the shared receptor IL-12Rβ1 to complete the ternary cytokine-receptor complex.

The p40 Subunit of IL-23 Mediates IL-12Rβ1 Binding

In the absence of direct structural evidence about where IL-12Rβ1 might be recruited to the cooperative IL-23:receptor complex, we leveraged the diverse molecular tools we created for this study and available mutagenesis studies and sought to expand and consolidate structural information from complexes of antibody fragments with IL-23. The IL-23:IL-23R:IL-12Rβ1 ternary complex has been hypothesized to follow the "site I-II-III" assembly paradigm inspired by seminal structural studies of the cytokine-receptor complex comprising IL-6,

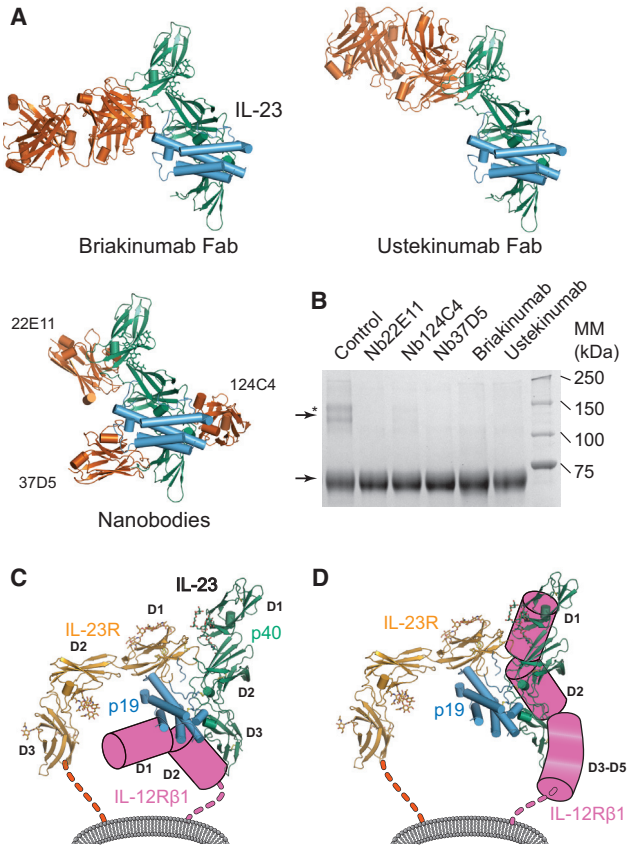

Figure 5. The IL-12Rβ1 Binding Epitope Maps to IL-12p40

(A) Cartoon representation of IL-23 structures (vermillion) in complex with antagonists: IL-23:briakinumab-Fab (reported herein); IL-23 in complex with three nanobodies (PDB: 4grw), IL-23:Ustekinumab-Fab (PDB: 3hmx).

(B) Cropped Coomassie-stained reducing SDS-PAGE gel of purified IL-23:IL-12Rβ1 complex crosslinked in the absence (control) or presence of IL-23 antagonists. Protein bands corresponding to crosslinked species (arrow with star) and IL-12Rβ1 in the absence of IL-23 antagonists (arrow) are indicated.

(C) Previously proposed model for the IL-23:receptor complex.

(D) Herein proposed model of the IL-23:IL-23R:IL-12Rβ1 ternary complex.

See also Figure S6.

IL-6Rα, and gp130 (Boulanger et al., 2003). This model places the helical bundle of IL-23p19 at the cross-roads of the assembly providing interaction sites for all cytokine and receptor modules concerned: site I for p40, site II for IL-12Rβ1, and site III for IL-23R. Our structural elucidation of the human IL-23:IL-23R complex has shown how sites I and III are utilized (Figures 1B and 1F).

To provide insights into how the shared receptor IL-12Rβ1 might interact with IL-23, we investigated the binding profile of the p40 subunit of IL-23 to IL-12Rβ1 by ITC. This yielded a very similar binding isotherm, affinity, and thermodynamic parameters as for the interaction of heterodimeric IL-23 with IL-12Rβ1 (Figures S5F and 4A). This provided direct evidence that the IL-23p19 is likely not involved in binding IL-12Rβ1 and that the low-affinity interaction between IL-23 and IL-12Rβ1 is exclusively mediated by the p40 subunit.

In light of this emerging new mode of binding, we further hypothesized that a careful selection of antagonistic molecules against IL-23 activity (Figure S6A) might provide additional clues about the binding epitope for IL-12Rβ1. We focused on the single domain VHH camelid antibodies 124C4, 22E11, and 37D5 (Saunders et al., 2009), which bind to sizeable albeit non-overlapping sites on IL-23, the therapeutic monoclonal antibody ustekinumab (Benson et al., 2011) binding to the D1-D2 junction of IL-12p40 (Luo et al., 2010), and the monoclonal antibody briakinumab (ABT-874) (Reich et al., 2011). As structural information about briakinumab was not available, we produced and purified the Fab fragment of briakinumab and determined the crystal structure of its complex with IL-23 and in the unbound form (Figure 5A; Table 1). Briakinumab targeted, like 22E11 and ustekinumab, the D1-D2 junction of IL-12p40 but is also tilted toward the IL-23R binding epitope in a manner incompatible with IL-23R binding (Figures 5A and S6B–S6D).

Next, we evaluated the ability of the five antibodies to abrogate the interaction between IL-23 and IL-12Rβ1. As the intrinsic low affinity of the IL-23:IL-12Rβ1 complex (Figure 4A) imposed limitations in the employment of conventional biophysical methods, we resorted to chemical cross-linking of IL-23:IL-12Rβ1 in the presence of each antibody followed by analyses of the cross-linked species by SDS-PAGE and western blotting. In the absence of steric hindrance, IL-23 and IL-12Rβ1 would be expected to produce chemical cross-links corresponding to a molecular species of ~120 kDa. We found that compared to the control, all five antibodies efficiently inhibited IL-23:IL-12Rβ1 complexes, providing evidence that their interaction epitopes are overlapping with IL-12Rβ1 binding (Figure 5B).

Thus, the conformational restraining of IL-23 upon binding of IL-23R to enable co-operative recruitment of IL-12Rβ1 appears to be manifested in two main ways. First, binding of IL-23R selects for a specific IL-12p40 conformation characterized by marked displacement of D1 and D3 with respect to D2 (Figure 2B). Second, the wedging of D1 of IL-23R close to the D1-D2 interface of IL-12p40 is poised to restrict the conformational degrees of freedom of IL-12p40. Indeed, the rather limited and loose interaction interface between IL-23R_{D1} and IL-12p40 observed in our IL-23:IL-23R binary complex might undergo compaction and extension upon recruitment of IL-12Rβ1 to the ternary complex. IL-12p40$_{D2D3}$ has been shown to be the minimal requirement for the interaction of IL-23 with IL-12Rβ1 (Schröder et al., 2015). Together, such structural and biochemical insights indicate that the p40 subunit of IL-23 is likely the major mediator of interactions with the shared receptor IL-12Rβ1.

Disease-Protecting Mutations due to SNP Can Be Mapped to the IL-23:IL-23R Complex

Our structural template for the IL-23:IL-23R complex provided a platform for rationalizing at the protein level the most frequent missense SNP identified in IL-23R and IL-23 via genome-wide association studies or targeted sequencing efforts. To this end we leveraged the curated browser of the Exome Aggregation Consortium (ExAC) (Lek et al., 2016). Nearly all most commonly occurring missense SNPs in the coding regions of the extracellular domain of IL-23R mapped to domains D2 and D3 far from the IL-23R:IL-23 interface (Table S2). A number of them have been linked to protective effects in IBD and/or Crohn's disease. For instance, a G149R substitution in IL-23R_{D2} is thought to exert its protective behavior in IBD and Crohn's disease via reduced

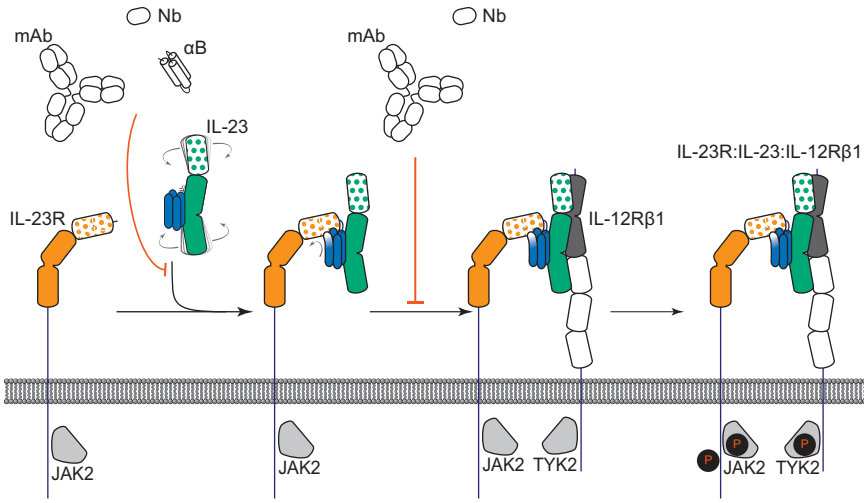

Figure 6. Assembly Mechanism of the Receptor Complex Mediated by IL-23

The signaling complex mediated by IL-23 proceeds via the sequential recruitment of the two cognate receptors, and involves conformational selection and restructuring of IL-23 by IL-23R to recruit IL-12Rβ1 with high affinity. Such cytokine-receptor ternary complex is poised to support phosphorylation of intracellular Jak2 and Tyk2 tyrosine kinases associated with the intracellular parts of the receptors, to initiate signaling cascades. Extracellular antagonism of such assemblies can be achieved at two different stages along the ternary complex itinerary depending on the specificity of IL-23 targeting. See also Figure S6A.

expression at the cell surface (Momozawa et al., 2011; Onodera et al., 2015; Rivas et al., 2011; Sivanesan et al., 2016). Nevertheless, at least one substitution, R86Q, does localize in the cytokine-binding domain of IL-23R and associates with a protective effect in IBD (Table S2; Momozawa et al., 2011). Furthermore, several SNPs correspond to amino acid substitutions within the region in IL-23p19 that interacts with IL-23R but also throughout the IL-12p40 subunit of IL-23 (Table S2). However, only a V298F substitution in D3 of IL-12p40 has been linked to a protective effect in IBD (Prescott et al., 2015). Whereas several amino acid substitutions resulting from SNPs in coding regions of IL-23 and IL-23R have been linked to protective roles in IBD and Crohn's disease, their impact at the molecular level currently remains unclear in light of the structural information we reported here.

DISCUSSION

IL-23 constitutes a major clinical target against widespread autoimmune and inflammatory diseases (Teng et al., 2015) and remains under intense investigation for its role in immunoregulation while structural and mechanistic insights into cytokine-receptor complexes of the IL-12 cytokine family have eluded the field for decades.

The findings we presented here enable a proposal for the assembly mechanism of the receptor complex mediated by IL-23 (Figure 6). The cornerstone thereof is the binary high-affinity complex of IL-23 with IL-23R. Despite featuring CHR extracellular domains, which cognate type I cytokine receptors typically employ for binding cytokines, IL-23R exclusively uses its N-terminal Ig domain to dock onto IL-23p19 as a primary interaction interface and to loosely contact IL-12p40 via a secondary interaction site. This direct visualization of the cytokine binding domain of IL-23R contrasts the rationale provided for the ability of a soluble version of human IL-23R_{CHR} (residues 124–313) produced in *E. coli* to inhibit the differentiation of Th17 cells and secretion of IL-17A in *in vitro* and *in vivo* studies (Guo et al., 2012). The epicenter of the IL-23:IL-23R interaction localizes at the N terminus of helix D in IL-23p19, which serves as a structural switch by undergoing restructuring to project the functional hotspot residue W156 to its active conformation. The IL-23:IL-23R binary complex is also an obligate mechanistic step for the recruitment of the shared receptor IL-12Rβ1, which otherwise has poor affinity to IL-23 and no measurable binding to IL-23R. The binding site for IL-12Rβ1 does not involve the IL-23p19 subunit and is thus distinct from the hitherto site II inspired by the IL-6:IL-6Rα:gp130 complex (Figure 6). We further note that IL-12p80, the dimeric disulfide-linked form of the IL-12p40 subunit, was shown to have both agonistic signaling properties as well as antagonistic behavior over a range of activities such as macrophage chemotaxis, inflammatory responses, and protective activity in a mycobacterial model, binds IL-12Rβ1 while lacking an α-helical subunit (Cooper and Khader, 2007). Together with recent studies which failed to identify mutations in IL-23p19 abrogating interactions with IL-12Rβ1 (Schröder et al., 2015), our findings point to a ternary assembly model that does not feature a IL-23p19:IL-12Rβ1 interface (site II), but a IL-12p40:IL-12Rβ1 interaction instead. Thus, our proposed assembly mechanism essentially segregates cognate and shared receptor binding to the helical (α) and non-helical (β) subunits of the heterodimeric cytokines in the IL-12 family, respectively (Figure 6).

Whereas the apparent cooperativity in the assembly of the IL-23:IL-23R:IL-12Rβ1 ternary complex is pronounced, as evidenced by the increase in affinity of IL-12Rβ1 to the IL-23:IL-23R complex, it does not appear to involve extensive receptor-receptor interactions between the extracellular domains of the two receptors contrary to other cytokine receptors (Felix et al., 2015; Spangler et al., 2015; Verstraete et al., 2017). In what appears to be a reversal of roles as dictated by current paradigms for cytokine-driven receptor activation, IL-23 becomes structurally activated by its high-affinity receptor, IL-23R, to enable recruitment of the shared receptor IL-12Rβ1 (Figure 6). Together, such insights may have implications as to what can be deduced for other members of the IL-12 family. Our present findings on IL-23 can be most readily extrapolated to the archetypal IL-12, given that the two cytokines share the IL-12p40 subunit, signal through IL-12Rβ1 as a common receptor, and exhibit pro-inflammatory activities. In particular, the conserved domain organization in IL-23R and IL-12Rβ2 in terms of an N-terminal Ig-domain preceding the CHR domains indicates that the two

receptors will likely share common cytokine binding principles. Of note is the conservation of the Ile-Cys-Gly amino acid sequence cassette in the G β strand of the Ig domains of IL-12Rβ2 and IL-23R, which in IL-23R accommodates the functionally critical W156 in IL-23p19. We would thus expect that Y189 in IL-12p35 would serve a similar role in IL-12 and that IL-12Rβ2 will be the high-affinity receptor for IL-12.

Over the last few years, evidence has been mounting that the IL-12 cytokine family displays expanded mix-and-match scenarios of cytokine subunits and utilization of signaling receptors covering a broad spectrum of immune responses (reviewed by Hasegawa et al., 2016). For instance, IL-39 has been recently introduced as a pro-inflammatory cytokine comprising the helical subunit IL-23p19 coupled to Epstein-Barr virus-induced protein 3 (EBI3) and has been proposed to signal via IL-23R and gp130 (Wang et al., 2016). Furthermore, IL-35, which comprises the helical IL-12p35 subunit coupled to EBI3, has been reported to mediate immunosuppressive responses through heterodimeric assemblies of IL-12Rβ2 and gp130, but also through homodimers of each receptor chain (Collison et al., 2012). It is currently unclear how our findings could help rationalize such receptor complexes mediated by IL-35. However, it is likely that higher-order assemblies might be necessary or that other co-receptors might be at play at the cell surface. Interestingly, IL-23 was recently shown to act on human $CD16^{+}MDL\text{-}1^{+}DAP12^{+}$ osteoclast precursors to induce osteoclast differentiation in inflammatory arthritis. This pathway instigated by IL-23 in myeloid cells uses DNAX activating protein of 12 kDa (DAP12) to recruit Spleen Tyrosine Kinase (SYK) and induce calcium-dependent activation of nuclear factor of activated T cells, cytoplasmic 1 (Shin et al., 2015).

Lastly, the structural and mechanistic insights we have presented here may further fuel efforts to antagonize signaling receptor assemblies mediated by IL-23 for therapeutic purposes. This is an area that has been extensively developed over the last decade via antibody and non-antibody protein scaffolds alike (Desmet et al., 2014; Hawkes et al., 2017; Ramamurthy et al., 2012). The need to differentiate therapeutic targeting of IL-23 from IL-12 has been called upon (Benson et al., 2011; Kulig et al., 2016). Indeed, the recent clinical approvals of guselkumab and tildrakizumab, two monoclonal antibodies against IL-23p19 for the treatment of plaque psoriasis (Blauvelt et al., 2017; Kopp et al., 2015; Reich et al., 2017), reflects such efforts for therapeutic differentiation. Thus, strategies addressing specifically the obligate IL-23:IL-23R binary complex or the functional hotspot centered at W156 in IL-23p19 may offer additional avenues to address the broad spectrum of diseases linked to IL-23.

STAR★METHODS

Detailed methods are provided in the online version of this paper and include the following:

- KEY RESOURCES TABLE
- CONTACT FOR REAGENT AND RESOURCE SHARING
- EXPERIMENTAL MODEL DETAILS
  - Mouse model for skin inflammation
- METHOD DETAILS
  - Plasmids, constructs, and cell lines for protein expression in mammalian cells
  - Protein expression in HEK293 and purification from conditioned media
  - Recombinant protein expression in *E.coli*
  - Crystal structure determination and refinement
  - Bio-layer Interferometry
  - Isothermal Titration Calorimetry
  - Multi-angle Laser Light Scattering (MALLS)
  - *In vitro* differentiation of naive T cells into Th17
  - RNA Extraction and Real-Time Quantitative PCR
  - Skin Histology
  - Protein crosslinking
- QUANTIFICATION AND STATISTICAL ANALYSIS
  - In-vivo experiments
  - ITC analysis
- DATA AVAILABILITY

SUPPLEMENTAL INFORMATION

Supplemental Information includes six figures and two tables and can be found with this article online at https://doi.org/10.1016/j.immuni.2017.12.008.

ACKNOWLEDGMENTS

We thank the staff of beam lines P14 (PETRAIII) and Proxima2A (SOLEIL) for beam time allocation and excellent technical support. We further thank Veronique De Backer (Ghent University Hospital) for technical support. Y.B. and S.D. are supported by pre-doctoral fellowships from the Flanders Agency for Innovation and Entrepreneurship (VLAIO-Flanders, Belgium). S.G. is supported by a postdoctoral fellowship from Research Foundation Flanders (FWO, Belgium). L.V.d.B., F.H., and M.D. are supported by the Ghent University Hospital Spearhead Initiative for Immunology Research. F.H. is supported by the Jeffrey Modell Foundation. I.E.A. acknowledges support from the NIAMS/NIH (grant AR62173) and a National Psoriasis Foundation Translational Research Grant. S.N.S. acknowledges research support from Research Foundation Flanders (FWO grant G0C2214N), the Hercules Foundation (no. AUGE-11-029), and the VIB.

AUTHOR CONTRIBUTIONS

Y.B. designed and performed recombinant protein production, biochemical, biophysical, and structural studies. Y.B. and S.N.S. analyzed data. R.M., S.D., and K.S. contributed to molecular tools and biochemical studies. L.B. and I.E.A. designed and performed studies employing the animal model of skin inflammation. L.V.d.B., M.D., F.H., S.G., and D.E. designed and performed *in vitro* cellular studies. Y.B. and S.N.S. wrote the manuscript with contributions from all authors. S.N.S. conceived and supervised the project.

DECLARATION OF INTERESTS

The authors declare no competing interests.

Received: June 30, 2017
Revised: October 15, 2017
Accepted: December 5, 2017
Published: December 26, 2017

REFERENCES

Adams, P.D., Afonine, P.V., Bunkóczi, G., Chen, V.B., Davis, I.W., Echols, N., Headd, J.J., Hung, L.W., Kapral, G.J., Grosse-Kunstleve, R.W., et al. (2010). PHENIX: a comprehensive Python-based system for macromolecular structure solution. Acta Crystallogr. D Biol. Crystallogr. *66*, 213–221.

Arakawa, A., Ruzicka, T., and Prinz, J.C. (2016). Therapeutic efficacy of interleukin 12/interleukin 23 blockade in generalized pustular psoriasis regardless of IL36RN mutation status. JAMA Dermatol. *152*, 825–828.

Aricescu, A.R., Lu, W., and Jones, E.Y. (2006). A time- and cost-efficient system for high-level protein production in mammalian cells. Acta Crystallogr. D Biol. Crystallogr. *62*, 1243–1250.

Benson, J.M., Sachs, C.W., Treacy, G., Zhou, H., Pendley, C.E., Brodmerkel, C.M., Shankar, G., and Mascelli, M.A. (2011). Therapeutic targeting of the IL-12/23 pathways: generation and characterization of ustekinumab. Nat. Biotechnol. *29*, 615–624.

Beyer, B.M., Ingram, R., Ramanathan, L., Reichert, P., Le, H.V., Madison, V., and Orth, P. (2008). Crystal structures of the pro-inflammatory cytokine interleukin-23 and its complex with a high-affinity neutralizing antibody. J. Mol. Biol. *382*, 942–955.

Blauvelt, A., Papp, K.A., Griffiths, C.E., Randazzo, B., Wasfi, Y., Shen, Y.K., Li, S., and Kimball, A.B. (2017). Efficacy and safety of guselkumab, an anti-interleukin-23 monoclonal antibody, compared with adalimumab for the continuous treatment of patients with moderate to severe psoriasis: Results from the phase III, double-blinded, placebo- and active comparator-controlled VOYAGE 1 trial. J. Am. Acad. Dermatol. *76*, 405–417.

Boulanger, M.J., Chow, D.C., Brevnova, E.E., and Garcia, K.C. (2003). Hexameric structure and assembly of the interleukin-6/IL-6 alpha-receptor/gp130 complex. Science *300*, 2101–2104.

Bricogne, G., Blanc, E., Brandl, M., Flensburg, C., Keller, P., Paciorek, W., Roversi, P., Sharff, A., Smart, O.S., Vonrhein, C., and Womack, T.O. (2016). Buster v.2.10.3 (Cambridge, United Kingdom: Global Phasing Ltd). https://www.globalphasing.com/buster/.

Collison, L.W., Delgoffe, G.M., Guy, C.S., Vignali, K.M., Chaturvedi, V., Fairweather, D., Satoskar, A.R., Garcia, K.C., Hunter, C.A., Drake, C.G., et al. (2012). The composition and signaling of the IL-35 receptor are unconventional. Nat. Immunol. *13*, 290–299.

Cooper, A.M., and Khader, S.A. (2007). IL-12p40: an inherently agonistic cytokine. Trends Immunol. *28*, 33–38.

D'Arcy, A., Villard, F., and Marsh, M. (2007). An automated microseed matrix-screening method for protein crystallization. Acta Crystallogr. D Biol. Crystallogr. *63*, 550–554.

Desmet, J., Verstraete, K., Bloch, Y., Lorent, E., Wen, Y., Devreese, B., Vandenbroucke, K., Loverix, S., Hettmann, T., Deroo, S., et al. (2014). Structural basis of IL-23 antagonism by an Alphabody protein scaffold. Nat. Commun. *5*, 5237.

Duerr, R.H., Taylor, K.D., Brant, S.R., Rioux, J.D., Silverberg, M.S., Daly, M.J., Steinhart, A.H., Abraham, C., Regueiro, M., Griffiths, A., et al. (2006). A genome-wide association study identifies IL23R as an inflammatory bowel disease gene. Science *314*, 1461–1463.

Eberl, G. (2016). Immunity by equilibrium. Nat. Rev. Immunol. *16*, 524–532.

Emsley, P., Lohkamp, B., Scott, W.G., and Cowtan, K. (2010). Features and development of Coot. Acta Crystallogr. D Biol. Crystallogr. *66*, 486–501.

Eswar, N., Webb, B., Marti-Renom, M.A., Madhusudhan, M.S., Eramian, D., Shen, M.Y., Pieper, U., and Sali, A. (2006). Comparative protein structure modeling using Modeller. Curr. Protoc. Bioinformatics *5*, 5–6.

Feldmeyer, L., Mylonas, A., Demaria, O., Mennella, A., Yawalkar, N., Laffitte, E., Hohl, D., Gilliet, M., and Conrad, C. (2017). Interleukin 23–helper T cell 17 axis as a treatment target for pityriasis rubra pilaris. JAMA Dermatol. *153*, 304–308.

Felix, J., De Munck, S., Verstraete, K., Meuris, L., Callewaert, N., Elegheert, J., and Savvides, S.N. (2015). Structure and assembly mechanism of the signaling complex mediated by human CSF-1. Structure *23*, 1621–1631.

Gaffen, S.L., Jain, R., Garg, A.V., and Cua, D.J. (2014). The IL-23-IL-17 immune axis: from mechanisms to therapeutic testing. Nat. Rev. Immunol. *14*, 585–600.

Grivennikov, S.I., Wang, K., Mucida, D., Stewart, C.A., Schnabl, B., Jauch, D., Taniguchi, K., Yu, G.Y., Osterreicher, C.H., Hung, K.E., et al. (2012). Adenoma-linked barrier defects and microbial products drive IL-23/IL-17-mediated tumour growth. Nature *491*, 254–258.

Gubler, U., Chua, A.O., Schoenhaut, D.S., Dwyer, C.M., McComas, W., Motyka, R., Nabavi, N., Wolitzky, A.G., Quinn, P.M., Familletti, P.C., et al. (1991). Coexpression of two distinct genes is required to generate secreted bioactive cytotoxic lymphocyte maturation factor. Proc. Natl. Acad. Sci. USA *88*, 4143–4147.

Guo, W., Luo, C., Wang, C., Zhu, Y., Wang, X., Gao, X., and Yao, W. (2012). Protection against Th17 cells differentiation by an interleukin-23 receptor cytokine-binding homology region. PLoS ONE *7*, e45625.

Hasegawa, H., Mizoguchi, I., Chiba, Y., Ohashi, M., Xu, M., and Yoshimoto, T. (2016). Expanding diversity in molecular structures and functions of the IL-6/IL-12 heterodimeric cytokine family. Front. Immunol. *7*, 479.

Hawkes, J.E., Chan, T.C., and Krueger, J.G. (2017). Psoriasis pathogenesis and the development of novel targeted immune therapies. J. Allergy Clin. Immunol. *140*, 645–653.

Heckman, K.L., and Pease, L.R. (2007). Gene splicing and mutagenesis by PCR-driven overlap extension. Nat. Protoc. *2*, 924–932.

Kabsch, W. (2010). Xds. Acta Crystallogr. D Biol. Crystallogr. *66*, 125–132.

Kopp, T., Riedl, E., Bangert, C., Bowman, E.P., Greisenegger, E., Horowitz, A., Kittler, H., Blumenschein, W.M., McClanahan, T.K., Marbury, T., et al. (2015). Clinical improvement in psoriasis with specific targeting of interleukin-23. Nature *521*, 222–226.

Korn, T., Bettelli, E., Oukka, M., and Kuchroo, V.K. (2009). IL-17 and Th17 cells. Annu. Rev. Immunol. *27*, 485–517.

Kulig, P., Musiol, S., Freiberger, S.N., Schreiner, B., Gyülveszi, G., Russo, G., Pantelyushin, S., Kishihara, K., Alessandrini, F., Kündig, T., et al. (2016). IL-12 protects from psoriasiform skin inflammation. Nat. Commun. *7*, 13466.

Langowski, J.L., Zhang, X., Wu, L., Mattson, J.D., Chen, T., Smith, K., Basham, B., McClanahan, T., Kastelein, R.A., and Oft, M. (2006). IL-23 promotes tumour incidence and growth. Nature *442*, 461–465.

Lee, J.S., Tato, C.M., Joyce-Shaikh, B., Gulen, M.F., Cayatte, C., Chen, Y., Blumenschein, W.M., Judo, M., Ayanoglu, G., McClanahan, T.K., et al. (2015). Interleukin-23-independent IL-17 production regulates intestinal epithelial permeability. Immunity *43*, 727–738.

Lek, M., Karczewski, K.J., Minikel, E.V., Samocha, K.E., Banks, E., Fennell, T., O'Donnell-Luria, A.H., Ware, J.S., Hill, A.J., Cummings, B.B., et al.; Exome Aggregation Consortium (2016). Analysis of protein-coding genetic variation in 60,706 humans. Nature *536*, 285–291.

Li, J., Wei, H., Krystek, S.R., Jr., Bond, D., Brender, T.M., Cohen, D., Feiner, J., Hamacher, N., Harshman, J., Huang, R.Y., et al. (2017). Mapping the energetic epitope of an antibody/interleukin-23 interaction with hydrogen/deuterium exchange, fast photochemical oxidation of proteins mass spectrometry, and alanine shave mutagenesis. Anal. Chem. *89*, 2250–2258.

Lin, Y.-C., Boone, M., Meuris, L., Lemmens, I., Van Roy, N., Soete, A., Reumers, J., Moisse, M., Plaisance, S., Drmanac, R., et al. (2014). Genome dynamics of the human embryonic kidney 293 lineage in response to cell biology manipulations. Nat. Commun. *5*, 4767.

Lowes, M.A., Suárez-Fariñas, M., and Krueger, J.G. (2014). Immunology of psoriasis. Annu. Rev. Immunol. *32*, 227–255.

Lubberts, E. (2015). The IL-23-IL-17 axis in inflammatory arthritis. Nat. Rev. Rheumatol. *11*, 415–429.

Luo, J., Wu, S.-J., Lacy, E.R., Orlovsky, Y., Baker, A., Teplyakov, A., Obmolova, G., Heavner, G.A., Richter, H.-T., and Benson, J. (2010). Structural basis for the dual recognition of IL-12 and IL-23 by ustekinumab. J. Mol. Biol. *402*, 797–812.

Lupardus, P.J., and Garcia, K.C. (2008). The structure of interleukin-23 reveals the molecular basis of p40 subunit sharing with interleukin-12. J. Mol. Biol. *382*, 931–941.

Maxwell, J.R., Zhang, Y., Brown, W.A., Smith, C.L., Byrne, F.R., Fiorino, M., Stevens, E., Bigler, J., Davis, J.A., Rottman, J.B., et al. (2015). Differential roles for interleukin-23 and interleukin-17 in intestinal immunoregulation. Immunity *43*, 739–750.

McCoy, A.J., Grosse-Kunstleve, R.W., Adams, P.D., Winn, M.D., Storoni, L.C., and Read, R.J. (2007). Phaser crystallographic software. J. Appl. Cryst. *40*, 658–674.

McGeachy, M.J., Chen, Y., Tato, C.M., Laurence, A., Joyce-Shaikh, B., Blumenschein, W.M., McClanahan, T.K., O'Shea, J.J., and Cua, D.J. (2009). The interleukin 23 receptor is essential for the terminal

differentiation of interleukin 17-producing effector T helper cells in vivo. Nat. Immunol. *10*, 314–324.

Momozawa, Y., Mni, M., Nakamura, K., Coppieters, W., Almer, S., Amininejad, L., Cleynen, I., Colombel, J.F., de Rijk, P., Dewit, O., et al. (2011). Resequencing of positional candidates identifies low frequency IL23R coding variants protecting against inflammatory bowel disease. Nat. Genet. *43*, 43–47.

Moutsopoulos, N.M., Zerbe, C.S., Wild, T., Dutzan, N., Brenchley, L., DiPasquale, G., Uzel, G., Axelrod, K.C., Lisco, A., Notarangelo, L.D., et al. (2017). Interleukin-12 and interleukin-23 blockade in leukocyte adhesion deficiency type 1. N. Engl. J. Med. *376*, 1141–1146.

Murphy, C.A., Langrish, C.L., Chen, Y., Blumenschein, W., McClanahan, T., Kastelein, R.A., Sedgwick, J.D., and Cua, D.J. (2003). Divergent pro- and anti-inflammatory roles for IL-23 and IL-12 in joint autoimmune inflammation. J. Exp. Med. *198*, 1951–1957.

Onodera, K., Arimura, Y., Isshiki, H., Kawakami, K., Nagaishi, K., Yamashita, K., Yamamoto, E., Niinuma, T., Naishiro, Y., Suzuki, H., et al. (2015). Low-frequency IL23R coding variant associated with Crohn's disease susceptibility in Japanese subjects identified by personal genomics analysis. PLoS ONE *10*, e0137801.

Oppmann, B., Lesley, R., Blom, B., Timans, J.C., Xu, Y., Hunte, B., Vega, F., Yu, N., Wang, J., Singh, K., et al. (2000). Novel p19 protein engages IL-12p40 to form a cytokine, IL-23, with biological activities similar as well as distinct from IL-12. Immunity *13*, 715–725.

Pardon, E., Laeremans, T., Triest, S., Rasmussen, S.G.F., Wohlkönig, A., Ruf, A., Muyldermans, S., Hol, W.G.J., Kobilka, B.K., and Steyaert, J. (2014). A general protocol for the generation of Nanobodies for structural biology. Nat. Protoc. *9*, 674–693.

Parham, C., Chirica, M., Timans, J., Vaisberg, E., Travis, M., Cheung, J., Pflanz, S., Zhang, R., Singh, K.P., Vega, F., et al. (2002). A receptor for the heterodimeric cytokine IL-23 is composed of IL-12Rbeta1 and a novel cytokine receptor subunit, IL-23R. J. Immunol. *168*, 5699–5708.

Prescott, N.J., Lehne, B., Stone, K., Lee, J.C., Taylor, K., Knight, J., Papouli, E., Mirza, M.M., Simpson, M.A., Spain, S.L., et al.; UK IBD Genetics Consortium (2015). Pooled sequencing of 531 genes in inflammatory bowel disease identifies an associated rare variant in BTNL2 and implicates other immune related genes. PLoS Genet. *11*, e1004955.

Ramamurthy, V., Krystek, S.R., Jr., Bush, A., Wei, A., Emanuel, S.L., Das Gupta, R., Janjua, A., Cheng, L., Murdock, M., Abramczyk, B., et al. (2012). Structures of adnectin/protein complexes reveal an expanded binding footprint. Structure *20*, 259–269.

Reeves, P.J., Callewaert, N., Contreras, R., and Khorana, H.G. (2002). Structure and function in rhodopsin: high-level expression of rhodopsin with restricted and homogeneous N-glycosylation by a tetracycline-inducible N-acetylglucosaminyltransferase I-negative HEK293S stable mammalian cell line. Proc. Natl. Acad. Sci. USA *99*, 13419–13424.

Reich, K., Langley, R.G., Papp, K.A., Ortonne, J.-P., Unnebrink, K., Kaul, M., and Valdes, J.M. (2011). A 52-week trial comparing briakinumab with methotrexate in patients with psoriasis. N. Engl. J. Med. *365*, 1586–1596.

Reich, K., Armstrong, A.W., Foley, P., Song, M., Wasfi, Y., Randazzo, B., Li, S., Shen, Y.K., and Gordon, K.B. (2017). Efficacy and safety of guselkumab, an anti-interleukin-23 monoclonal antibody, compared with adalimumab for the treatment of patients with moderate to severe psoriasis with randomized withdrawal and retreatment: Results from the phase III, double-blind, placebo- and active comparator-controlled VOYAGE 2 trial. J. Am. Acad. Dermatol. *76*, 418–431.

Rivas, M.A., Beaudoin, M., Gardet, A., Stevens, C., Sharma, Y., Zhang, C.K., Boucher, G., Ripke, S., Ellinghaus, D., Burtt, N., et al.; National Institute of Diabetes and Digestive Kidney Diseases Inflammatory Bowel Disease Genetics Consortium (NIDDK IBDGC); United Kingdom Inflammatory Bowel Disease Genetics Consortium; International Inflammatory Bowel Disease Genetics Consortium (2011). Deep resequencing of GWAS loci identifies independent rare variants associated with inflammatory bowel disease. Nat. Genet. *43*, 1066–1073.

Sambrook, J., and Russell, D.W. (2006). Calcium-phosphate-mediated transfection of eukaryotic cells with plasmid DNAs. CSH Protoc. *2006*, https://doi.org/10.1101/pdb.prot3871.

Saunders, M.J.S., Blanchetot, C., Rommelaere, H., Vercammen, J., and De Haard, J.J.W. (2009). Amino acid sequences directed against heterodimeric cytokines and/or their receptors and polypeptides comprising the same. European patent EP 2 650 311 A2, filed November 27, 2008; published October 16, 2013.

Schröder, J., Moll, J.M., Baran, P., Grötzinger, J., Scheller, J., and Floss, D.M. (2015). Non-canonical interleukin 23 receptor complex assembly: p40 protein recruits interleukin 12 receptor β1 via site II and induces p19/interleukin 23 receptor interaction via site III. J. Biol. Chem. *290*, 359–370.

Shin, H.-S., Sarin, R., Dixit, N., Wu, J., Gershwin, E., Bowman, E.P., and Adamopoulos, I.E. (2015). Crosstalk among IL-23 and DNAX activating protein of 12 kDa-dependent pathways promotes osteoclastogenesis. J. Immunol. *194*, 316–324.

Shirouzono, T., Chirifu, M., Nakamura, C., Yamagata, Y., and Ikemizu, S. (2012). Preparation, crystallization and preliminary X-ray diffraction studies of the glycosylated form of human interleukin-23. Acta Crystallogr. Sect. F Struct. Biol. Cryst. Commun. *68*, 432–435.

Sidobre, S., and Kronenberg, M. (2002). CD1 tetramers: a powerful tool for the analysis of glycolipid-reactive T cells. J. Immunol. Methods *268*, 107–121.

Sivanesan, D., Beauchamp, C., Quinou, C., Lee, J., Lesage, S., Chemtob, S., Rioux, J.D., and Michnick, S.W. (2016). IL23R (Interleukin 23 Receptor) variants protective against inflammatory bowel diseases (IBD) display loss of function due to impaired protein stability and intracellular trafficking. J. Biol. Chem. *291*, 8673–8685.

Skiniotis, G., Boulanger, M.J., Garcia, K.C., and Walz, T. (2005). Signaling conformations of the tall cytokine receptor gp130 when in complex with IL-6 and IL-6 receptor. Nat. Struct. Mol. Biol. *12*, 545–551.

Spangler, J.B., Moraga, I., Mendoza, J.L., and Garcia, K.C. (2015). Insights into cytokine-receptor interactions from cytokine engineering. Annu. Rev. Immunol. *33*, 139–167.

Suzuki, E., Maverakis, E., Sarin, R., Bouchareychas, L., Kuchroo, V.K., Nestle, F.O., and Adamopoulos, I.E. (2016). T cell-independent mechanisms associated with neutrophil extracellular trap formation and selective autophagy in IL-17A-mediated epidermal hyperplasia. J. Immunol. *197*, 4403–4412.

Teng, M.W.L., Bowman, E.P., McElwee, J.J., Smyth, M.J., Casanova, J.-L., Cooper, A.M., and Cua, D.J. (2015). IL-12 and IL-23 cytokines: from discovery to targeted therapies for immune-mediated inflammatory diseases. Nat. Med. *21*, 719–729.

Verstraete, K., Remmerie, B., Elegheert, J., Lintermans, B., Haegeman, G., Vanhoenacker, P., Van Craenenbroeck, K., and Savvides, S.N. (2011). Inducible production of recombinant human Flt3 ectodomain variants in mammalian cells and preliminary crystallographic analysis of Flt3 ligand-receptor complexes. Acta Crystallogr. Sect. F Struct. Biol. Cryst. Commun. *67*, 325–331.

Verstraete, K., van Schie, L., Vyncke, L., Bloch, Y., Tavernier, J., Pauwels, E., Peelman, F., and Savvides, S.N. (2014). Structural basis of the proinflammatory signaling complex mediated by TSLP. Nat. Struct. Mol. Biol. *21*, 375–382.

Verstraete, K., Peelman, F., Braun, H., Lopez, J., Van Rompaey, D., Dansercoer, A., Vandenberghe, I., Pauwels, K., Tavernier, J., Lambrecht, B.N., et al. (2017). Structure and antagonism of the receptor complex mediated by human TSLP in allergy and asthma. Nat. Commun. *8*, 14937.

Vignali, D.A.A., and Kuchroo, V.K. (2012). IL-12 family cytokines: immunological playmakers. Nat. Immunol. *13*, 722–728.

Wang, X., Lupardus, P., Laporte, S.L., and Garcia, K.C. (2009). Structural biology of shared cytokine receptors. Annu. Rev. Immunol. *27*, 29–60.

Wang, X., Wei, Y., Xiao, H., Liu, X., Zhang, Y., Han, G., Chen, G., Hou, C., Ma, N., Shen, B., et al. (2016). A novel IL-23p19/Ebi3 (IL-39) cytokine mediates inflammation in Lupus-like mice. Eur. J. Immunol. *46*, 1343–1350.

Wolf, S.F., Temple, P.A., Kobayashi, M., Young, D., Dicig, M., Lowe, L., Dzialo, R., Fitz, L., Ferenz, C., Hewick, R.M., et al. (1991). Cloning of cDNA for natural killer cell stimulatory factor, a heterodimeric cytokine with multiple biologic effects on T and natural killer cells. J. Immunol. *146*, 3074–3081.

Zhang, L., Li, J., Li, L., Zhang, J., Wang, X., Yang, C., Li, Y., Lan, F., and Lin, P. (2014). IL-23 selectively promotes the metastasis of colorectal carcinoma cells with impaired Socs3 expression via the STAT5 pathway. Carcinogenesis *35*, 1330–1340.

Zhao, J., Liu, Y.-H., Reichert, P., Pflanz, S., and Pramanik, B. (2010). Glycosylation analysis of interleukin-23 receptor: elucidation of glycosylation sites and characterization of attached glycan structures. J. Mass Spectrom. *45*, 1416–1425.

STAR★METHODS

KEY RESOURCES TABLE

REAGENT or RESOURCE	SOURCE	IDENTIFIER
Antibodies		
Human IL-12/IL-23 p40 antibody (goat polyclonal)	R&D	Cat # AF309; RRID: AB_10718110 (Batch # CEOF0115101)
Human IL-12 Rb1 antibody (goat polyclonal)	R&D	Cat # AF839; RRID: AB_355649 (Batch # CCQ021509A)
Donkey Anti-Goat IgG DyLight 800	Invitrogen	Cat # SA5-10092; RRID: AB_2556672 (Batch # QB1982323)
Mouse anti-CD3ε	eBioscience	Cat # 16-0032-86; RRID: AB_468853
Anti-CD3ε (V500-conjugated)	BD Biosciences	Cat # 560771; RRID: AB_1937314
Anti-CD4 (FITC-conjugated)	BD Biosciences	Cat # 553651; RRID: AB_394971
Anti-CD8α (PE-conjugated)	eBioscience	Cat # 12-0081-83; RRID: AB_465531
Anti-CD19 (violetFluor 450-conjugated)	Tonbo Biosciences	Cat # 75-0193; RRID: AB_2621940
Mouse anti-CD28	eBioscience	Cat # 16-0281-85; RRID: AB_468922
Anti-CD44 (APC-Cy7-conjugated)	eBioscience	Cat # 47-0441-82; RRID: AB_1272244
Anti-CD62L (PE-Cy7-conjugated)	Tonbo Biosciences	Cat # 60-0621; RRID: AB_2621855
Bacterial and Virus Strains		
E. coli WK6	VIB Nanobody Service Facility	https://corefacilities.vib.be/nsf
Chemicals, Peptides, and Recombinant Proteins		
BS^3	Thermo Scientific	Cat # 21585 (Batch # QG220572)
hIL-23, hIL-12p40, hIL-23R, hIL-23R_{CHR}, hIL-12Rβ1, mIL-23, mIL-23 mutants, briakinumab Fab, ustekinumab Fab, Nb 124C4, Nb 22E11, Nb 37D5	This paper	N/A
Anti-CD1d tetramer (APC-labeled)	Produced in house (Sidobre and Kronenberg, 2002)	N/A
Mouse IL-23 R Fc chimera	R&D	Cat # 1686-MR-050 (Batch # ICQ0713121)
Aldara® Antineoplastic Agent Imiquimod 5% Unit Dose	Medicis Dermatologics	Cat # 99207026012
Formaldehyde Solution	Fisher Chemical	Cat # M1004965000
Hematoxylin Solution	Sigma-Aldrich	Cat # GHS116
Eosin Y solution, aqueous	Sigma-Aldrich	Cat # HT110216
Critical Commercial Assays		
Anti-human IgG Fc Capture biosensors	fortéBIO	Cat # 18-5060 (Batch # 1611032)
Brilliant III Ultra-Fast SYBR® Green QPCR Master Mix	Agilent technologies	Cat # 600882
Mouse IL-17A ELISA	eBioscience	Cat # 88-7371-22
Mouse IL-22 ELISA	eBioscience	Cat # 88-7422-22
Omniscript RT Kit	QIAGEN	Cat # 205113
RNeasy Mini Kit	QIAGEN	Cat # 74106
Deposited Data		
IL-23:IL-23R:Nb22E11	This paper	PDB: 5mzv
IL-23	This paper	PDB: 5mxa
briakinumab FAb	This paper	PDB: 5n2k
IL-23:briakinumab FAb	This paper	PDB: 5njd
Experimental Models: Cell Lines		
Human: HEK293T	Lin et al., 2014	N/A
Human: HEK293S *MGAT1*$^{-/-}$	Reeves et al., 2002	N/A

(*Continued on next page*)

Continued

REAGENT or RESOURCE	SOURCE	IDENTIFIER
Experimental Models: Organisms/Strains		
Mouse: C57BL/6J	The Jackson Laboratory	JAX: 000664; RRID: IMSR_JAX:000664
Oligonucleotides		
Primer: *B2m* Forward: CTGCTACGTAACACAGTTCCACCC	Suzuki et al., 2016	N/A
Primer: *B2m* Reverse: CATGATGCTTGATCACATGTCTCG	Suzuki et al., 2016	N/A
Primer: *Krt16* Forward: TATCCACTCCTCCTCACAGC	Suzuki et al., 2016	N/A
Primer: *Krt16* Reverse: GCTGGTTGAACCTTGCTCCT	Suzuki et al., 2016	N/A
Primer: *S100a8* Forward: TGCGATGGTGATAAAAGTGG	Suzuki et al., 2016	N/A
Primer: *S100a8* Reverse: GGCCAGAAGCTCTGCTACTC	Suzuki et al., 2016	N/A
Primer: *S100a9* Forward: CACAGTTGGCAACCTTTATG	Suzuki et al., 2016	N/A
Primer: *S100a9* Reverse: CAGCTGATTGTCCTGGTTTG	Suzuki et al., 2016	N/A
Recombinant DNA		
pHLsec parental vector	Aricescu et al., 2006	N/A
pCDNA4/TO parental vector	Invitrogen	Cat # V102020
pMECS parental vector	VIB Nanobody Service Facility	https://corefacilities.vib.be/nsf
Software and Algorithms		
Astra (version 6.1.6)	Wyatt	https://www.wyatt.com
BZ-Analyzer software	Keyence	https://www.keyence.com
Data Analysis software (version 9.0.0.14)	FortéBIO	https://www.fortebio.com
GraphPad Prism Software, version 6	GraphPad	https://www.graphpad.com
PEAQ-ITC analysis software (version 1.1.0.1262)	Malvern	https://www.malvern.com/en
Phenix	Adams et al., 2010	http://www.phenix-online.org/; RRID: SCR_014224
XDS	Kabsch 2010	http://xds.mpimf-heidelberg.mpg.de/; RRID: SCR_015652

CONTACT FOR REAGENT AND RESOURCE SHARING

Further information and requests for resources and reagents should be directed to and will be fulfilled by the Lead Contact, Savvas Savvides (savvas.savvides@ugent.be) The HEK293S *MGAT1*$^{-/-}$ cell line and derivatives thereof cannot be freely distributed as some rights remain with the cell line developers.

EXPERIMENTAL MODEL DETAILS

Mouse model for skin inflammation

8 week old male C57BL/6J mice were purchased from Jackson Laboratories (Sacramento, CA). The University of California at Davis Institutional Animal Care and Use Committee approved all animal protocols. Mice were intradermally injected with PBS, or 10 μg of recombinant mIL-23 or mIL-23 mutants daily at opposing sides of shaved dorsal skin for 4 consecutive days. The IL-23 dose was empirically determined to cause optimal and reproducible skin inflammation in mice (Figure S4). Naive mice and mice treated with a daily topical dose of 35 mg of IMQ cream (5%) (Aldara; Medicis Dermatologics) on the dorsal skin were used as negative and positive controls respectively.

METHOD DETAILS

Plasmids, constructs, and cell lines for protein expression in mammalian cells

For testing expression of protein constructs and transient expression in HEK293 cells, constructs were cloned into the pHLsec plasmid (Aricescu et al., 2006). For generating stable cell lines, selected constructs were cloned into the pCDNA4TO (Thermo Fisher scientific) plasmid. For ease of cloning an EcoRI-site was inserted 3′ of the AflII site in the multi cloning site (MCS) of the pCDNA4 plasmid to resemble the pHLsec MCS.

The reference sequences of the cDNA encoding for hIL-12p40 residues Met1-Ser328 (NM_002187.2), hIL-23p19 residues Met1-Pro189 (NM_016584.2), mIL-12p40 residues Met1-Ser335 (NM_001303244.1) and mIL-23p19 residues Met1-Ala196 (NM_031252.2) were synthesized by Geneart and were a kind gift from Complix NV. However, to allow for cloning into the pHLsec vector, the AAT codon for Asn248 in the hIL-12p40 sequence was replaced with AAC. Human and mouse IL-12p40 were cloned

without any purification tags. Human and mouse IL-23p19 were cloned in frame with a C-terminal hexahistidine tag. Mutants of mIL-23p19 were generated using overlap extension PCR (Heckman and Pease, 2007), employing a PCR protocol adapted for Q5 polymerase (NEB) and allowing the final PCR to first run for 5 extra cycles without primers.

Sequence optimized DNA encoding for the reference sequences of IL-23R residues Met1-Glu317 (full extra cellular domains (ECD)) or Gly122-Glu317 (ECD D2D3) (NP_653302.2) and IL-12Rβ1 (full ECD) residues Met1-Arg544 (NP_005526.1) were purchased from Genscript. IL-23R was cloned in frame with a C-terminal Factor-Xa site followed by a hexahistidine tag, the D2D3 construct was further cloned in frame with an N-terminal chicken RTPμ-like secretion signal. IL-12Rβ1 was cloned in frame with a C-terminal FactorXa site followed by an AviHis tag.

Sequence optimized DNA encoding the light and heavy chains of ustekinumab Fab and briakinumab Fab were purchased from IDT as GBlocks. The N-terminal signal peptide sequences were exchanged for a chicken RTPμ-like signal peptide sequence. The light chains were cloned without any purification tag. The heavy chains were cloned in frame with a C-terminal thrombin site followed by a hexahistidine tag.

For the generation of monoclonal cell lines the constructs in pCDNA4TO plasmids were linearized in the *AMPR* gene by digestion with either Pvu1 or Sca1. The linearized DNA was purified using ethanol precipitation. Prior to transfection the medium of the HEK293S *MGAT1*$^{-/-}$ *TETR* cells was exchanged for HEPES buffered MEM supplemented with 0.1 mM chloroquine. The cells were transfected according to the calcium phosphate method (Sambrook and Russell, 2006). For the heterodimeric hIL-23 plasmids encoding each chain were co-transfected in a 1:1 ratio. Transformants were selected by supplementing the growth medium with 200 mg/l Zeocin. Individual colonies were picked and tested for target protein expression upon tetracycline induction using SDS-PAGE and western blot.

Protein expression in HEK293 and purification from conditioned media

All protein production in mammalian cells was done via the adherent HEK293S *MGAT1*$^{-/-}$ *TETR* cell line with the exception of the antibody Fab fragments, murine IL-23 and mutants thereof, which were expressed in adherent HEK293T cells. HEK293 cells were maintained in DMEM + 10% FCS and were supplemented with 50 mg/l Zeocin for stable cell lines. The growth medium was exchanged to DMEM supplemented with 3.6 mM valproic acid upon protein expression. To induce expression in stable cell lines 2 mg/l tetracycline was additionally added to the medium.

Transient expression in HEK293 cells was achieved using polyethylenimine as transfection reagent (Aricescu et al., 2006). For the heterodimeric Fab fragments and mIL-23, plasmids encoding for each chain were co-transfected in a 1:1 ratio. Conditioned medium was harvested from the HEK293 cultures once the cell morphology and integrity assessed by light microscopy deteriorated. Medium was clarified via centrifugation and filtered through a 0.22 μm filter prior to chromatographic steps.

The standard chromatography running buffer used during protein purification and SEC-MALLS experiments was HBS (20 mM HEPES pH 7.4, 150 mM NaCl). IMAC elution buffer was HBS supplemented with 250 mM imidazole, 5% (v/v) glycerol and 0.05% (v/v) Tween20. His-tagged proteins were captured using Immobilized Metal Affinity Chromatography IMAC (cOmplete His-tag purification resin, Roche) and polished via size exclusion chromatography (SEC) (HiLoad 16/600 superdex 75 or 200, GE Lifesciences). The AviHis tag of IL-12Rβ1 was removed by overnight digestion of the purified protein with Bovine Factor Xa (Prozyme) at 287 K in HBS supplemented with 2mM $CaCl_2$. To remove any undigested protein and the enzyme, the digestion mixture was loaded onto a HiTrap benzamidine FFcolumn (GE lifesciences) in series with a HisTrap FF column (GE Lifesciences). The flowthrough containing tagless IL-12Rβ1 was polished on SEC. The AviHis tag of the heavy chain of the ustekinumab and briakinumab Fabs were removed by overnight digestion of the purified protein with human Thrombin (Novagen) at 287 K in HBS supplemented with 2 mM $CaCl_2$. Undigested protein was removed via IMAC. The flow-through containing tag-free Fab fragments was polished on SEC. For the murine IL-23 and mutants thereof used for animal studies, endotoxin levels were measured using a Endosafe PTS limulus amebocyte lysate assay (Charles river) and were below 5 EU/mg.

Recombinant protein expression in *E.coli*

DNA encoding nanobodies were sequence-optimized for expression in *E. coli* and were purchased from IDT as GBlocks. The sequences were cloned in a variant of the pMECS vector whereby the nanobody construct was in frame with a N-terminal PelB signal peptide sequence and a C-terminal StrepTagII tag. Single domain VHH camelid antibodies were expressed as described by (Pardon et al., 2014) in *E. coli* WK6. The capture step using IMAC was replaced by a Streptactin based affinity-purification according to manufacturer's protocol (IBA Lifesciences) and the protein was polished using SEC (HiLoad 16/600 Superdex 75).

Crystal structure determination and refinement

For crystals of the IL23:IL23R:Nb22E11 complex, the complex was assembled and purified via SEC. Glycans were trimmed by overnight enzymatic digestion with Jack bean α-mannosidase (Prozyme) in HBS supplemented with 2 mM $ZnCl_2$ and 50 mM Bis-Tris pH 6.5. After overnight digestion, the complex was further purified via SEC and concentrated to 7 mg/ml. Commercial sparse matrix sitting drop crystallization screens were set up using a Mosquito liquid handling robot (TTP Labtech) using a 100 nL protein mixed with 100 nL mother liquor geometry in SwissSci 96-well triple drop plates. Plates were incubated at 287 K. Hits were optimized in both sitting and hanging drop format. An original hit in the JCSG+ screen (0.2M MgCl2 0.1M Tris pH 7 10% PEG8000) was optimized to 0.2M $MgCl_2$ 0.1M Tris pH 6.6 11% (w/v) PEG8000 in hanging drop format. Crystals were cryoprotected in mother liquor supplemented with 20% ethylene glycol prior to being cryo-cooled in liquid nitrogen. Diffraction data was collected at 100 K at the P14 microfocus beam line at PETRA III, Hamburg.

Diffraction data was integrated and using XDS (Kabsch, 2010). The anisotropic datasets were truncated and rescaled using the STARANISO server. Initial phases were obtained using maximum likelihood molecular replacement in Phaser (McCoy et al., 2007) using a composite model of the IL-23 (PDB: 4oe8) 22E11 nanobody (PDB: 4grw) complex. Structure building and refinement was performed iteratively in COOT (Emsley et al., 2010) and Phenix.refine (Adams et al., 2010) or BUSTER (Bricogne et al., 2016). The IL-23R structure was built from scratch into the electron density. Two isotropic atomic displacement parameters (ADP, one for main-chain atoms and one for sidechain atoms) were refined per residue together with rigid body harmonic displacement parameters described by a translation libration screw-rotation (TLS) model. TLS groups were determined in Phenix and glycans were assigned to their closest protein group. Higher resolution local torsion-angle restraints were imposed for IL-23 (PDB: 4oe8) and the nanobody 22E11 (PDB: 4grw).

For IL-23:briakinumab-Fab crystals the complex was purified via SEC and concentrated to 9 mg/ml. Screens were set up and optimized as described above. An original hit in the JCSG+ and Index screen (2 M $(NH_4)_2SO_4$, 100 mM BisTris pH 5.5) was optimized to 2 M $(NH_4)_2SO_4$, 100 mM BisTris pH 6 in sitting drop format. Crystals were cryoprotected in 90% (v/v) saturated $(NH_4)_2SO_4$, 10% (v/v) 1 M BisTris pH 6 prior to being cryocooled in liquid nitrogen. Diffraction data was collected at 100 K at the P14 microfocus beam line at PETRA III, Hamburg. The data were processed as described above with the exception that the "BEAM_DIVERGENCE" parameter had to be doubled in XDS, greatly improving the dataset consistency. Initial phases were obtained from a dataset of an isomorphous crystal diffracting to 4.8Å using maximum likelihood molecular replacement in Phaser. Search models were IL-23 (PDB: 4oe8) and a briakinumab homology model created in Modeler (Eswar et al., 2006) split into constant and variable domains without CDR loops. Structure building and refinement was performed iteratively in COOT and Phenix.refine or BUSTER. One overall isotropic ADP parameter was refined together with a TLS model. One TLS group was assigned per chain. Higher resolution local torsion-angle restraints were imposed for IL23 (PDB: 4oe8) and the briakinumab Fab (structure reported in this paper) as well as local torsion angle non-crystallographic symmetry (NCS) restraints.

For briakinumab Fab crystals the protein was concentrated to 19 mg/ml and a pH versus PEG3350 concentration or $(NH_4)_2SO_4$ concentration screen was set up in hanging drop format. A single crystal from an optimized crystallization hit (21.6% (w/v) PEG 3350 40 mM Glycine pH 9.5) was used to prepare a seed stock (D'Arcy et al., 2007) at a nominal 1/1000 dilution using a PTFE seed bead (Hampton Research). This seed stock was used to set up micro-seeded matrix screens of the PEG-ION HT sparse matrix screen and an optimization screen of the original hit with 600 nL drops (200 nL protein, 100 nL seed stock and 300 nL mother liquor). Crystals developed faster and in more drops of the optimization screen of the original hit compared to the non-seeded screen. An isomorphous crystal also grew in condition A12 (200 mM NH_4I, 20% (w/v) PEG 3350 pH 6.2) of the PEGION HT screen (Hampton Research). This crystal was cryoprotected in 80% (v/v) mother-liquor supplemented with 20% (v/v) ethylene glycol prior to being cryo-cooled in liquid nitrogen.

Diffraction data were collected at 100 K at the P14 microfocus beam line at PETRA III, Hamburg. The data was processed as described above with the difference that the dataset was isotropic and was not processed with the STARANISO server. Initial phases were obtained using maximum likelihood molecular replacement in Phaser. The briakinumab homology model, split in constant and variable domains without CDR loops as described above, was used as search model. Structure building and refinement was performed as described above. Individual isotropic ADP parameters were refined together with a TLS model. The TLS groups were assigned to each domain. Local torsion angle non-crystallographic symmetry (NCS) restraints were imposed.

Crystals of glycosylated human IL-23 produced in HEK293S *MGAT1*$^{-/-}$ *TETR* cells were grown as previously described (Shirouzono et al., 2012). IL-23 was concentrated to 6 mg/ml and a narrow pH versus PEG1000 concentration screen was set up around the published condition (18% (w/v) PEG 1000, 200 mM Li_2SO_4, 100 mM sodium citrate, 100 mM sodium phosphate pH 4.2) in both hanging- and sitting-drop geometry using 200 nL drops (100 nL protein mixed with 100 nL mother liquor). A crystal grown in hanging drop with 19.5% (w/v) PEG1000, 100 mM sodium citrate, 100 mM sodium phosphate pH 4.4, 200 mM Li_2SO4 was cryoprotected in mother liquor supplemented up to 25% (w/v) PEG1000 prior to being cryocooled in liquid nitrogen. Diffraction data was collected at 100 K at the P14 microfocus beam line at PETRA III, Hamburg.

The data were processed as described above with the difference that the dataset was isotropic and was not processed with the STARANISO server. Initial phases were obtained using maximum likelihood molecular replacement in Phaser using the IL-23 model from PDB entry 4oe8. Structure building and refinement was performed as described above. Individual isotropic ADP parameters were refined together with a TLS model. TLS groups were assigned by Phenix. Final refinement of all structures was done against the datasets that were not processed by the STARANISO server. The original datasets were deposited in the PDB together with the corresponding structure coordinates.

Bio-layer Interferometry

The binding kinetics and dissociation constant of IL-23, and mutants thereof, toward murine IL-23R were characterized by biolayer interferometry (BLI). Binding assays were performed using an Octet Red 96 machine (FortéBIO) in assay buffer (20 mM HEPES pH 7.4, 300 mM NaCl, 0.05% (w/v) BSA, 0.05% (v/v) Tween 20) at 303 K. Lyophilized mouse IL-23R Fc fusion protein (R&D Systems) was reconstituted in PBS to 0.1 mg/ml as recommended by the manufacturer. mIL-23R Fc was immobilized at 5 μg/ml in PBS onto anti-human IgG Fc capture biosensors (FortéBIO) until an optical shift of ~0.5 nm was achieved. To correct for system artifacts, system drift, and non-specific binding to the biosensors (the latter was apparent at higher analyte concentrations) the experiments were set up in a double referenced geometry. Additional control biosensors were therefore not coated with mIL-23R-Fc. After equilibrating the biosensors in assay buffer, the biosensors were dipped in a 3-fold dilution series (517 nM, 172 nM, 57 nM, 19 nM, 6 nM, 2 nM, and

0 nM as a negative control) of cytokine for 300 s during the association phase followed by a 600 s dissociation phase in assay buffer. All biosensors were regenerated after each cycle in 10 mM glycine pH 1.75. After subtraction of the control sensorgrams, a 1:1 binding model was fitted to each dilution series. Assay design and data acquisition were performed using the BLI Data acquisition software 9.0.0.49 (FortéBIO) and data analysis was performed using the Data Analysis software 9.0.0.14 (FortéBIO).

Isothermal Titration Calorimetry

Prior to all measurements all protein pairs were buffer matched on SEC in standard SEC running buffer (20 mM HEPES pH 7.4, 150 mM NaCl). Experiments were carried out using a VP-ITC MicroCalorimeter except for the IL-23 in IL-23R_{CHR} and the IL-12Rβ1 in IL-23R titrations, both of which were carried out using a MicroCal PEAQ-ITC instrument. The experiments were conducted at 310 K. Injection spacing was chosen to allow for the signal to get back to a stable baseline. Data were analyzed using the PEAQ-ITC analysis software (version 1.1.0.1262, Malvern) and fit using a "one set of sites" model. In case of experiments involving free IL-23R in the cell or syringe, the concentration of IL-23R was corrected to allow for a 1:1 stoichiometry.

Multi-angle Laser Light Scattering (MALLS)

Protein samples of 100 μl at approximately 1mg/ml were injected onto a Superdex increase 10/300 GL column (GE Lifesciences) connected in line to a UV-detector (Shimadzu), a miniDawnTReos (Wyatt) multi-angle laser light scattering detector and an optilab T-Rex (Wyatt) refractometer thermostated at 298 K. The refractive increment value (dn/dc) was adapted to reflect the expected glycosylation of the protein using the formula

$$\frac{dn}{dc} = \frac{MW_{protein} * 0.185mL/g + MW_{glycan} * 0.15mL/g}{MW_{total}},$$

whereby the MW_{glycan} is estimated at 1.2 kDa per N-linked glycan. IL-23 has one clear N-linked glycan in available crystal structures, IL-23R has 7 visible N-linked glycans in our crystal structure, IL-12Rβ1 has 6 predicted N-linked glycosylation sites and the Fab fragments have none.

Band broadening was corrected for using reference measurements of BSA (Pierce). Data analysis was carried out using the Astra 6.1.6 software and standard deviations were calculated in the Excel software.

In vitro differentiation of naive T cells into Th17

Conventional naive CD4+ T cells obtained from spleens of C57BL/6J 8-week old male mice were FACS sorted to over 99% purity after being stained with PE-Cy7-conjugated anti-CD62L (Tonbo Biosciences), FITC-conjugated anti-CD4 (BD Biosciences), V500-conjugated anti-CD3ε (BD Biosciences), violetFluor 450-conjugated anti-CD19 (Tonbo Biosciences), PE-conjugated anti-CD8α (eBioscience), APC-Cy7-conjugated anti-CD44 (eBioscience) and APC-conjugated anti-CD1d tetramer (Sidobre and Kronenberg, 2002). After purification, cells were cultured in RPMI containing 10% fetal calf serum, glutamine, non-essential amino acids, sodium pyruvate, 2-mercaptoethanol, penicillin and streptomycin. Naive CD4+ T cells were seeded in a 96-well U-bottom plate (1×10^5 cells/well) coated with anti-CD3ε mAb (3 μg/ml; eBioscience) and then further activated with soluble anti-CD28 mAb (5 μg/ml; eBioscience). Culture medium was supplemented with increasing concentrations (0, 1.5625, 6.25, 25, 100 ng/ml or 0-1.7 nM) of recombinant mouse IL-23 or IL-23 mutants to induce Th17 differentiation. After 4 days of stimulation, concentrations of IL-17A and IL-22 in culture supernatants were detected by ELISA (eBioscience).

RNA Extraction and Real-Time Quantitative PCR

Total RNA was extracted using the RNeasy mini kit (QIAGEN), following the manufacturer's instructions. The purity of the RNA was assessed by the ratio of absorbance at 260 and 280cnm. RNA preparation was reverse-transcribed using the Omniscript RT Kit (QIAGEN). The resultant cDNA were amplified by qPCR using Brilliant III Ultra-Fast SYBR QPCR (Agilent technologies) with the following primers:: Mouse *B2m*, 5′-CTGCTACGTAACACAGTTCCACCC-3′ and 5′-CATGATGCTTGATCACATGTCTCG-3′; mouse *Krt16*, 5′- TATCCACTCCTCCTCACAGC −3′ and 5′- GCTGGTTGAACCTTGCTCCT-3′; mouse *S100a8*, 5′- TGCGATGGTGATAA AAGTGG-3′ and 5′- GGCCAGAAGCTCTGCTACTC −3′; mouse S100a9, 5′- CACAGTTGGCAACCTTTATG-3′ and 5′- CAGCTGATT GTCCTGGTTTG-3′. Experiments were performed in triplicate and gene expression levels were normalized to the Beta-2-Microglobulin housekeeping gene.

Skin Histology

Dorsal skin was collected and fixed in 4% formaldehyde (Fisher Chemical), embedded in paraffin, cut longitudinally into 5-μm sections and stained with hematoxylin and eosin (Sigma-Aldrich). Images were acquired using a Keyence BZ 9000 microscope. Thickness of epidermis was measured by using the BZ-Analyzer software (Keyence) and data shown represents the average of 10 measurements per section, with 2 sections per mouse.

Protein crosslinking

The ability of IL-23 antagonists to disrupt the IL-23:IL-12Rβ1 complex was assessed using chemical crosslinking. The crosslinking experiment was performed in HBS at RT. 4 μl (40 pmol) of purified IL-23:IL-12Rβ1 complex was crosslinked with 1 μl (500 pmol) freshly dissolved BS3 (Thermo Scientific) for 30 min in the absence (control) or presence of 2 μl (80 pmol) of IL-23 antagonists. The reaction

was quenched by adding 1 μl 1M TRIS pH 9. The resulting sample was analyzed on SDS-PAGE under reducing conditions and stained with Coomassie blue. The presence of both IL-12p40 and IL-12Rβ1 in the crosslinked species was ascertained by western blot using polyclonal anti human IL-12p40 and anti-human IL-12 Rβ1 primary antibodies (R&D).

QUANTIFICATION AND STATISTICAL ANALYSIS

In-vivo experiments

Significance of observed differences was determined by one-way ANOVA followed by Holm-Sidak's multiple comparisons test. Analysis was performed with the GraphPad Prism Software, version 6.

ITC analysis

Fitted values are reported with their fitting errors as reported by the MicroCal PEAQ-ITC Analysis software version 1.1.0.1262. The errors (also called standard errors) in the fit parameters are calculated as square root of respective diagonal elements of variance-covariance matrix (calculated from partial derivatives of the fitted function with respect to the fitted parameters). The errors calculated with default fitting procedure are then scaled (multiplied) with the square root of the reduced chi-square.

DATA AVAILABILITY

Crystallographic coordinates and structure factors have been deposited to the Protein Data Bank (www.rcsb.org) as follows: human IL-23:IL-23R:Nb22E11 complex (PDB: 5mzv), unbound human IL-23 (PDB: 5mxa), IL-23:Briakinumab^{Fab} complex (PDB: 5njd), and Briakinumab^{Fab} (PDB: 5n2k).